

# Exploring Structural Sparsity of Coil Images from 3-Dimensional Directional Tight Framelets for SENSE Reconstruction\*

Yan-Ran Li, Raymond H. F. Chan, Lixin Shen, Xiaosheng Zhuang, Risheng Wu, Yijun Huang, Junwei Liu<sup>†</sup>

**Abstract.** Each coil image in a parallel magnetic resonance imaging (pMRI) system is an imaging slice modulated by the corresponding coil sensitivity. These coil images, structurally similar to each other, are stacked together as a 3-dimensional (3D) image data and their sparsity property can be explored via 3D directional Haar tight framelets. The features of the 3D image data from the 3D framelet systems are utilized to regularize sensitivity encoding (SENSE) pMRI reconstruction. Accordingly, a so-called SENSE3d-algorithm is proposed to reconstruct images of high quality from the sampled  $K$ -space data with a high acceleration rate by decoupling effects of the desired image (slice) and sensitivity maps. Since both the imaging slice and sensitivity maps are unknown, this algorithm repeatedly performs a slice-step followed by a sensitivity-step by using updated estimations of the desired image and the sensitivity maps. In the slice-step, for the given sensitivity maps, the estimation of the desired image is viewed as the solution to a convex optimization problem regularized by the sparsity of its 3D framelet coefficients of coil images. This optimization problem, involved data from the complex field, is solved by a primal-dual-three-operator splitting (PD3O) method. In the sensitivity-step, the estimation of sensitivity maps is modelled as the solution to a Tikhonov-type optimization problem that favours the smoothness of the sensitivity maps. This corresponding problem is nonconvex, and could be solved by a forward-backward splitting method. Experiments on real phantoms and in-vivo data show that the proposed SENSE3d-algorithm can explore the sparsity property of the imaging slices and efficiently produce reconstructed images of high quality with reducing aliasing artifacts caused by high acceleration rate, additive noise, as well as the inaccurate estimation of each coil sensitivity. To provide a comprehensive picture of the overall performance of our SENSE3d model, we provide quantitative index (HaarPSI) and comparisons to some deep learning methods such as VarNet and fastMRI-UNet.

**Key words.** pMRI and SENSE, Structural sparsity, Directional Haar framelet regularization, 3D features, PD3O, HaarPSI, U-Net, VarNet, fastMRI-UNet.

**AMS subject classifications.** 42C15, 42C40, 58C35, 65D18, 65D32

**1. Introduction and motivation.** The Magnetic Resonance Imaging (MRI) is a common technique in medical diagnosis. Most of the MRI sequences in use today are based on a “spin-warp” imaging scheme [7], where the spatial information with phase was encoded successively by varying the amplitude of the gradients of the radio frequency pulses. Such a scheme is a Fourier-transform MRI

\*Submitted to editors DATE.

**Funding:** The work of R. Chan was supported in part by HKRGC Grants Nos. CUHK14301718, NCityU214/19, CityU11301120, CityU11309922, C1013-21GF, and CityUGrant9380101. The work of L. Shen was supported in part by the National Science Foundation under grant DMS-1913039 and DMS-2208385, and Syracuse CUSE grant. The work of X. Zhuang was supported in part by the Research Grants Council of Hong Kong (Project no. CityU 11309122 and CityU 11302023).

<sup>†</sup>Y.-R. Li, R. Wu, Y. Huang and J. Liu are with College of Computer Science and Software Engineering, Shenzhen University, Shenzhen, 518060, China, Emails: lyran@szu.edu.cn, sunrise\_wu@foxmail.com, 2070276106@email.szu.edu.cn, 2200271023@email.szu.edu.cn; L. Shen is with Department of Mathematics, Syracuse University, Syracuse, NY 13244, Email: lshen03@syr.edu; R. Chan is with Department of Mathematics, City University of Hong Kong, Tat Chee Avenue, Kowloon Tong, Hong Kong SAR, China; Hong Kong Centre for Cerebro-Cardiovascular Health Engineering, Email: raymond.chan@cityu.edu.hk; X. Zhuang is with Department of Mathematics, City University of Hong Kong, Tat Chee Avenue, Kowloon Tong, Hong Kong, Emails: xzhuang7@cityu.edu.hk.

method that produces data in the spatial frequency space, known as the  $K$ -space. The spatial frequency domain content of the imaged object is encoded directly into  $g(k_x, k_y)$ , the magnetic resonance (MR) signal at spatial frequencies  $k_x$  and  $k_y$  in the  $x$ - and  $y$ -directions, respectively. In the  $K$ -space of the form  $g(k_x, k_y) = \iint s(x, y)u(x, y)e^{2\pi i x k_x} e^{2\pi i y k_y} dx dy$ , where  $s(x, y)$  is the *coil sensitivity function* and  $u(x, y)$  is the *spatial spin density function* of the original object such as bones, joints, and soft tissues. The decoding process involves the inverse Fourier transform to obtain the target MRI image  $u(x, y)$  for medical diagnosis purpose. In order to reproduce accurate reconstruction images, enough phase-encoding steps are needed to cover sufficient positions in the  $K$ -space. Hence, the MRI scans typically take longer time.

Parallel MRI (pMRI) technique is a hardware solution used in clinical applications to shorten the imaging time. It utilizes a set of receiver coils surrounding the target object to detect the MR signals. To accelerate the data acquisition procedure, the pMRI system uses reconstruction algorithms to predict the imaging structures of the original MR signal only from collected partial (downsampling)  $K$ -space data [9, 28]. This downsampling process significantly reduces the scan time, but the resulting pMRI reconstruction is ill-posed and requires regularization techniques to improve the quality of the MRI images [6]. Most pMRI techniques can be categorized as the image domain methods (e.g., SENSE), the  $K$ -space methods (e.g., GRAPPA), and their hybrids. In this paper, we focus on the SENSE-based pMRI method.

**1.1. SENSE-based pMRI reconstruction.** SENSE is a technique that allows a reduction in scan time through the use of multiple receiver coils in an imaging mode [28]. More precisely, in a pMRI process, we denote  $g_\ell$  the acquired  $K$ -space signal received by the  $\ell$ th coil by

$$(1.1) \quad g_\ell = PF(s_\ell \odot u) + \eta_\ell, \quad \ell = 1, \dots, L,$$

where  $L$  is the total number of coils,  $u \in \mathbb{R}^n$  is the vectorization form of the desired image representing the density of the hydrogen protons in tissues (this is for convenience of presentation, in practice,  $u$  is kept as a 2D image),  $F \in \mathbb{C}^{n \times n}$  is the discrete Fourier transform matrix,  $P \in \mathbb{R}^{n \times n}$  is a sampling matrix,  $\eta_\ell \in \mathbb{C}^n$  is the additive noise, and  $s_\ell \in \mathbb{C}^n$  is the sensitivity vector of the  $\ell$ th coil. Here,  $a \odot b$  is the Hadamard product of  $a$  and  $b$  with the same dimension. The sampling matrix  $P$  is diagonal with diagonal entries being 0 or 1. The observation model in (1.1) shows that the coils simultaneously measure the same region but with downsampling process in order to increase the scan speed.

When the sensitivity vectors  $s_\ell$  are available, we can write (1.1) in a compact form. To this end, let us define  $S_\ell := \text{diag}(s_\ell)$  for  $\ell = 1, \dots, L$  and

$$(1.2) \quad g := \begin{bmatrix} g_1 \\ \vdots \\ g_L \end{bmatrix}, S := \begin{bmatrix} S_1 \\ \vdots \\ S_L \end{bmatrix}, \eta := \begin{bmatrix} \eta_1 \\ \vdots \\ \eta_L \end{bmatrix}, M := \begin{bmatrix} PFS_1 \\ \vdots \\ PFS_L \end{bmatrix}.$$

With these notation, a unified representation of the acquired signal  $g_\ell$  in equation (1.1) is given by

$$(1.3) \quad g = Mu + \eta,$$

where  $g \in \mathbb{C}^{Ln}$ ,  $M \in \mathbb{C}^{Ln \times n}$ , and  $\eta \in \mathbb{C}^{Ln}$ .

Regularization techniques are often adopted to regularize the ill-posed problem (1.3). In what follows, we address the issues related to dealing with the inverse problem (1.3).

69 **1.2. Structural sparsity of coil images explored via 3D directional framelets.** Regu-  
 70 larization techniques on the 2D target image are commonly used for the SENSE methods to improve  
 71 the reconstruction quality. One typical example is the framelet (or wavelet) regularization model of  
 72 the form:

$$73 \quad (1.4) \quad \min \left\{ \frac{1}{2} \|Mu - g\|_2^2 + \|\Gamma W_{2D}u\|_1 : u \in \mathbb{R}^n \right\},$$

74 where  $\Gamma$  is a diagonal matrix with non-negative diagonal elements, and  $W_{2D}$  is the matrix associated  
 75 with a 2D framelet transform. Model (1.4) uses fixed (pre-estimated) coil sensitivity maps  $s_\ell$  and  
 76 regularizes on the framelet coefficients of the underlying target image  $u$ . It applies  $W_{2D}$  on each coil  
 77 image or target slice to produce sparse coefficient sequences, and process them one by one. We refer  
 78 to (1.4) as *SENSE2d-U model*.

79 The pMRI system has multiple coil images and each coil image containing parts of the information  
 80 of the target slice which are correlated with each others. For example, Fig. 1(a) shows the four coil  
 81 images of size  $512 \times 512$  from (the inverse discrete Fourier transform of) the corresponding full  $K$ -  
 82 space data  $g_\ell$  acquired by an MRI machine. It can be seen that the intensity of each coil image is  
 83 uneven and the intensities of the coil images are mismatched. Without considering their correlated  
 84 information together, it could lead to poor quality of the reconstruction image, e.g., see Fig. 2(c).

85 Observe that the coil images are sparse in two aspects: (1) each coil image contains essentially  
 86 smooth areas separated by edge features, and (2) the coil images are structurally similar to each others  
 87 with areas of different high intensity. How can we explore the sparsity within each coil image and  
 88 among different coil images? In view of the fact that the coil images are from the same target slice  
 89 modulated via multiple coils in different positions, it is thus natural and reasonable to stack and view  
 90 them as a 3D signal (data) of size  $512 \times 512 \times 4$ , see Fig. 1(b). We can then use a 3D directional  
 91 framelet system to get a more harmonic image and explore its sparsity. More precisely, using a 3D  
 92 Haar lowpass filter  $a^H$  in a 3D directional framelet system  $\text{DHF}_3^3 = \{a^H; b_x, b_y, b_{xy}, b_{x,y}, b_{aux}\}$  (see  
 93 Section 2), which plays the role of averaging, the neighbouring coil images with labels (1) – (4) are  
 94 averaged, which produces a 3D signal of four images, labelled as (1 + 2), (2 + 3), (3 + 4), and (4 + 1),  
 95 having more areas with less intensive difference, see Fig. 1(c). In the second level, the 3D signal, which  
 96 is the stacked version of the four images (1 + 2), (2 + 3), (3 + 4), and (4 + 1), is further averaged by  
 97 the upsampled lowpass filter, which produces a 3D signal of four images with label (1 + 2 + 3 + 4)  
 98 having almost the same intensity level of brightness (see Fig. 1(d)). The lowpass filtering by the 3D  
 99 tight framelet filter greatly utilizes the correlated information among the coil images as well within the  
 100 coil images to produce images with harmonic intensity level, which in turn facilitates the production of  
 101 the sparse representation of the 3D signal by the directional high-pass filters  $b_x, b_y, b_{xy}, b_{x,y}$  (playing  
 102 the role of differencing) of the 3D framelet system  $\text{DHF}_3^3$ . The full 3D directional framelet system  
 103  $\text{DHF}_3^3$  plays the central role in our 3D SENSE-based pMRI regularization model.

104 In view of the above discussion, it is natural to consider the following 3D framelet regularization  
 105 pMRI model:

$$106 \quad (1.5) \quad \min \left\{ \frac{1}{2} \|Mu - g\|_2^2 + \|\Gamma W_{3D}Su\|_1 : u \in \mathbb{R}^n \right\},$$

107 where  $W_{3D}$  is the matrix associated with a 3D tight framelet transform. The differences of the regu-  
 108 larization terms in (1.4) and (1.5) are obvious. The regularization term  $\|\Gamma W_{2D}u\|_1$  in (1.4) measures

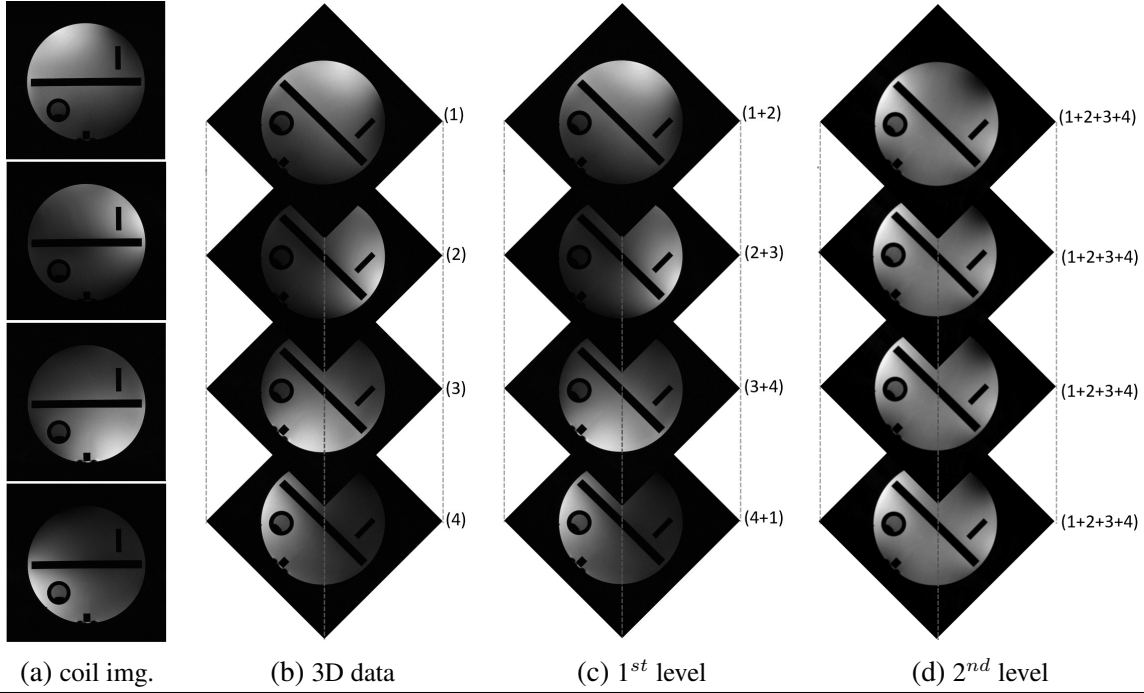


**Figure 1.** 2-Level 3D directional Haar tight framelet lowpass filtering. (a) Four  $512 \times 512$  coil images. (b) The 4 coil images, labeled as (1), (2), (3), and (4), are stacked as a 3D image data of size  $512 \times 512 \times 4$ . (c) First level lowpass filtering of the 3D image by a 3D Haar lowpass filter  $a^H$ . This results in images obtained from averaging within each coil image and across coil images. (d) Second level low-pass filtering of the middle 3D image. Each slice of the second level filtered 3D image is the same, which is the average of the 4 coil images.

109 the sparsity with the  $\ell_1$  norm for the desired image  $u$  under a 2D tight framelet transform while the  
 110 regularization term  $\|\Gamma W_{3D} S u\|_1$  in (1.5), as motivated by Fig. 1(c), measures the sparsity with the  $\ell_1$   
 111 norm of *all* coil images  $S u$  under a 3D framelet transform. If  $S$  is pre-estimated, then we shall call  
 112 such a model in (1.5) the *SENSE3d-U model*.

113 **1.3. The SENSE3d-algorithm and the SENSE3d model.** The sensitivity vectors  $s_\ell$  are  
 114 spatially nonuniform and are unknown. The difficulty of model (1.5) is to find an estimate of  $u$   
 115 under the scenario that  $s_\ell$  are unknown and the acquired  $K$ -space signals  $g_\ell$  are incomplete. For  
 116 the SENSE2d-U model and SENSE3d-U models, each sensitivity map  $s_\ell$  is usually pre-estimated as  
 117 follows: the blurry coil image  $\tilde{g}_\ell = F^{-1} g_\ell$  is acquired by the inverse Fourier transform of the center  
 118  $K$ -space data, and then the sensitivity for each coil is estimated as  $s_\ell = \tilde{g}_\ell / \sqrt{|\tilde{g}_1|^2 + \dots + |\tilde{g}_L|^2}$ .  
 119 However, both models with such pre-estimated coil selectivity maps usually do not perform well. See  
 120 Figs. 2(c) and (d).

121 We treat both  $u$  and the sensitivity vectors  $s_\ell$  as our *target solutions* in our proposed optimization  
 122 models and propose a so-called SENSE3d-algorithm to find the estimates of  $u$  and  $s_\ell$  iteratively. The  
 123 basic steps in the SENSE3d-algorithm are the ‘Slice-step’ and the ‘Sensitivity-step’:

124 (1) Slice-step: Find an estimate of the slice image  $u$  from the observed  $K$ -space signals  $g_\ell$  and  
 125 the guesses of  $s_\ell$ . The reconstruction of  $u$  from (1.3) is obtained by solving an optimization

126 model (see (1.5) or (3.3)) regularized by a 3D directional Haar tight framelet system.  
 127 (2) Sensitivity-step: Update the sensitivity vectors  $s_\ell$ , for  $\ell = 1, 2, \dots, L$ , from the observed  
 128  $K$ -space signal  $g_\ell$  and the estimate of  $u$ . The target image  $u$  is obtained by using a smooth  
 129 assumption on  $s_\ell$ . Once we have an approximation to the target image  $u$ , we can use it  
 130 to update the sensitivities that are the solution of a Tikhonov-type optimization model (see  
 131 (3.10)).  
 132 The above two steps are alternately repeated until stability is reached. To avoid additional notation,  
 133 details on the ‘Slice-step’ and the ‘Sensitivity-step’ will be discussed in Section 3. We shall call the  
 134 model using the SENSE3d-algorithm, that is (3.3)+(3.10) detailed in Section 3, together with our  
 135 DHF<sub>3</sub> framelet regularization, the *SENSE3d model*.

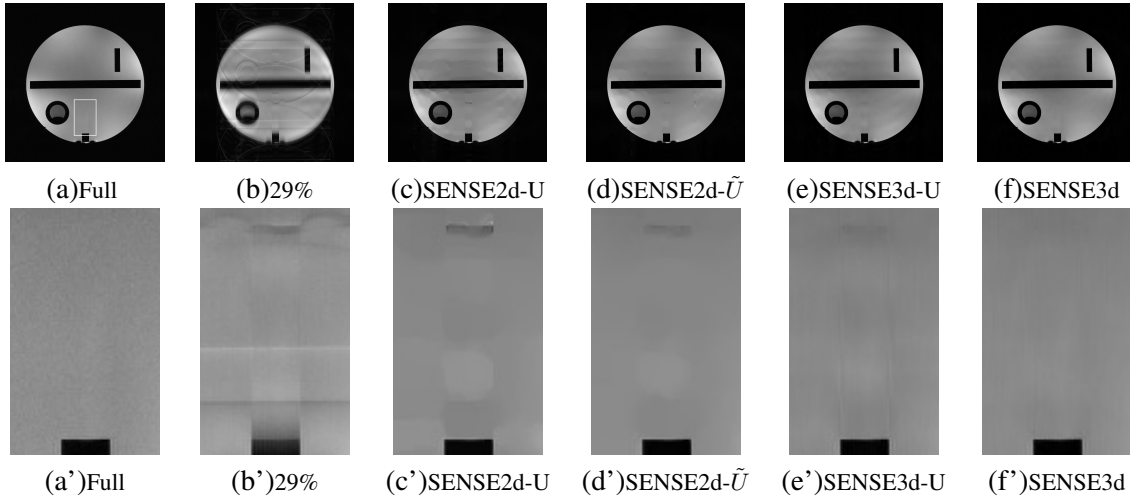


**Figure 2.** (a) Reference SoS image by the full  $K$ -space data with to-be zoom-in area (the white rectangle); (b) SoS image by the four coil images with 29%  $K$ -space data on uniform sampling model as shown in Fig. 3(a); (c) The SENSE2d-U model (1.4) by pMRI algorithm FADHFA [21]; (d) The SENSE2d- $\tilde{U}$  which is the pMRI algorithm FADHFA using the sensitivity map estimated by our SENSE3d algorithm; (e) The SENSE3d-U model (1.5); and (f) The SENSE3d model (3.3)+(3.10). (a')–(f'): The zoom-in part of (a)–(f) of the same white rectangle area, respectively.

136 The *SENSE3d* model significantly improves the quality of the reconstruction target image  $u$ . One  
 137 can see the performance comparisons among the three models *SENSE2d-U*, *SENSE3d-U*, *SENSE3d*,  
 138 and *SENSE2d- $\tilde{U}$* , from Fig. 2. We use the phantom images with four coil images of size  $512 \times 512$ .  
 139 The  $K$ -space data of each coil is partially sampled according to the sampling model in Fig. 3(a) (29%  
 140 of the  $K$ -space with 24 auto calibration signal (ACS) lines). Fig. 2(b) is the SoS (sum-of-square)  
 141 image of the four downsampled coil images, which is obviously blurred with aliasing artifacts. The  
 142 MRI images reconstructed by *SENSE2d-U*, *SENSE2d- $\tilde{U}$* , *SENSE3d-U*, and *SENSE3d* are shown in  
 143 Figs. 2(c), (d), (e), and (f), respectively.

144 Comparing *SENSE3d-U* and *SENSE2d-U* model, one can see that *SENSE3d-U* model is better  
 145 in reducing the aliasing artifacts than that of *SENSE2d-U* model. As shown by the zoom-in parts,  
 146 the ‘‘Column’’ and the ‘‘Row’’ aliasing artifacts in Fig. 2(c') (*SENSE2d-U*) are mostly reduced by  
 147 the *SENSE3d-U* model in Fig. 2(e'). This confirms that the correlated futures of coil images by our  
 148 3D framelet system can efficiently suppress the artifacts by the downsampling operation in the  $K$ -space  
 149 domain. Comparing the *SENSE3d-U* model (without iterating updating of  $s_\ell$ ) and the *SENSE3d* model

150 (with iterating updating of  $s_\ell$ ), one can see from Figs. 2(e) and (f) that the reconstruction target image  $u$   
 151 by the *SENSE3d* does not have aliasing artifacts. The zoom-in parts in Figs. 2(e') and (f') show that the  
 152 *SENSE3d* model can get more accurate sensitivity to reconstruct better target images. Aliasing artifacts  
 153 in Fig. 2(e') are removed in Fig. 2(f') via our *SENSE3d* models. Finally, the *SENSE2d- $\tilde{U}$* , which is  
 154 the pMRI algorithm FADHFA using the sensitivity map estimated by our *SENSE3d* algorithm, shows  
 155 its improvement over *SENSE2d-U*, but it is still not as good as *SENSE3d-U*.

156 The performance of the *SENSE3d-U* model from the above is better than that of the *SENSE2d-U*  
 157 model while the performance of *SENSE3d* model is better than that of the *SENSE3d-U* model. The  
 158 reconstructed and sensitivity models in (3.3) and (3.10), respectively, are interacted with each other  
 159 to improve the quality of the MRI images by our DHF<sub>3</sub><sup>3</sup> framelet regularization. We demonstrate in  
 160 Section 4 with more experimental results for comparing with other state-of-the-art methods.

161 **1.4. Contributions and structure.** The contributions of the paper mainly lie in the following  
 162 three aspects. First, we introduce the use of 3D directional Haar framelets for the regularization of the  
 163 pMRI reconstruction under the SENSE-based method. In view of the correlated information among  
 164 coil images, the 3D directional Haar framelet system DHF<sub>3</sub><sup>3</sup> not only produces coil images with har-  
 165 monic pixel intensity but also greatly facilitates the exploration of the sparsity within each coil image  
 166 as well as the sparsity across coil images. Secondly, we propose a so-called *SENSE3d*-algorithm to  
 167 estimate the target image and the coil sensitivity maps iteratively. Unlike some 2D models and 3D  
 168 models that are using pre-estimated coil sensitivity maps, our *SENSE3d*-algorithm treats both the un-  
 169 derlying image  $u$  and the coil sensitivity maps  $s_\ell$  as our target solutions of some optimization models  
 170 by 3D regularization. Such a *SENSE3d*-algorithm together with our 3D directional Haar framelet reg-  
 171 ularization gives rise to our *SENSE3d* model, which provides high quality reconstruction images with  
 172 excellent performance improvement. Finally, we provide detailed step-by-step procedures for solving  
 173 the optimization problems appeared in the Slice-step and Sensitivity-step of the *SENSE3d*-algorithm.  
 174 Moreover, we gives theoretical justifications on the convergence analysis of the two iterative algo-  
 175 rithms for the Slice-step and Sensitivity-step, respectively.

176 The structure of the paper is as follows. In Section 2, we discuss 3D directional Haar framelets  
 177 for our pMRI regularization. In Section 3, we present our optimization model for the pMRI SENSE  
 178 reconstruction and develop the numerical algorithms to solve the model iteratively. In Section 4, we  
 179 conduct numerical experiments on the comparisons of several state-of-the-art methods using various  
 180 MRI data. Conclusions and further remarks are given in the last section. Some proofs are postponed  
 181 to the appendix.

182 **2. 3-Dimensional directional Haar framelets filter banks.** In what follow, we briefly  
 183 discuss the 3D directional Haar tight framelet filter bank DHF<sub>3</sub><sup>3</sup> for our 3D SENSE-based pMRI reg-  
 184 ularization model.

185 By  $l_0(\mathbb{Z}^d)$  we denote the set of all finitely supported sequences. A *mask/filter*  $h = \{h(k)\}_{k \in \mathbb{Z}^d} : \mathbb{Z}^d \rightarrow \mathbb{C}$   
 186 on  $\mathbb{Z}^d$  is a sequence in  $l_0(\mathbb{Z}^d)$  whose *Fourier series* is defined to be  $\hat{h}(\xi) := \sum_{k \in \mathbb{Z}^d} h(k)e^{-ik \cdot \xi}$   
 187 for  $\xi \in \mathbb{R}^d$ . We denote  $\delta$  as the *Dirac sequence* such that  $\delta(0) = 1$  and  $\delta(k) = 0$  for all  
 188  $k \in \mathbb{Z}^d \setminus \{0\}$ , and  $\delta_\gamma := \delta(\cdot - \gamma)$  for  $\gamma \in \mathbb{Z}^d$ . Throughout the paper, we assume the tight framelets  
 189 are *dyadic dilated*, that is, the *dilation matrix* is  $2I_d$  with  $I_d$  the  $d \times d$  identity matrix. For filters  
 190  $a, b_1, \dots, b_m \in l_0(\mathbb{Z}^d)$ , we say that a filter bank  $\{a; b_1, \dots, b_m\}$  is a (*d-dimension dyadic*) *tight*

191 *framelet filter bank* if  $\forall \xi \in \mathbb{R}^d, \omega \in \{0, 1\}^d$ ,

$$192 \quad (2.1) \quad \widehat{a}(\xi)\overline{\widehat{a}(\xi + \pi\omega)} + \sum_{\iota=1}^m \widehat{b}_\iota(\xi)\overline{\widehat{b}_\iota(\xi + \pi\omega)} = \delta(\omega),$$

193 where  $\bar{x}$  denotes the complex conjugate of  $x \in \mathbb{C}$ . The filter  $a$  is a *lowpass filter* satisfying  $\widehat{a}(0) = 1$   
 194 while  $b_\iota$ 's are the *highpass filters* satisfying  $\widehat{b}_\iota(0) = 0$ . Such a filter bank  $\{a; b_1, \dots, b_m\}$  corre-  
 195 sponds to a *framelet system*  $\{\varphi; \psi_1, \dots, \psi_m\}$  through the refinement relations:  $\widehat{\varphi}(2\xi) = \widehat{a}(\xi)\widehat{\varphi}(\xi)$  and  
 196  $\widehat{\psi}_\iota(2\xi) = \widehat{b}_\iota(\xi)\widehat{\varphi}(\xi)$ , where the *Fourier transform* is defined to be  $\widehat{f}(\xi) := \int_{\mathbb{R}^d} f(x)e^{-ix \cdot \xi} dx$  for a  
 197 function  $f \in L_1(\mathbb{R}^d)$ . For more details, we refer to [11].

198 Now consider  $a^H = 2^{-d} \sum_{\gamma \in \{0,1\}^d} \delta_\gamma$  to be the  $d$ -dimensional Haar lowpass filter. Define the set  
 199  $\{b_1, \dots, b_m\} := \{2^{-d}(\delta_{\gamma_1} - \delta_{\gamma_2}) : \gamma_1, \gamma_2 \in \{0,1\}^d \text{ and } \gamma_1 < \gamma_2\}$  of highpass filters. Here  $\gamma_1 < \gamma_2$   
 200 is understood in the sense of lexicographical order. Then we have  $m = \binom{2^d}{2} = 2^{d-1}(2^d - 1)$ . It was  
 201 shown in [12] (see also [19, 38] for the generalization) that  $\{a^H; b_1, \dots, b_m\}$  is a tight framelet filter  
 202 bank such that all the highpass filters  $b_1, \dots, b_m$  have only two taps and exhibit  $\frac{1}{2}(3^d - 1)$  directions in  
 203 dimension  $d$ . In particular, for  $d = 1$ , the tight framelet filter bank is just the standard Haar orthogonal  
 204 wavelet filter bank  $\text{DHF}_1 := \{a^H; b\}$  with  $a^H = \frac{1}{2}(\delta_0 + \delta_1)$  and  $b = \frac{1}{2}(\delta_0 - \delta_1)$ . For  $d = 2$ ,  
 205 the corresponding tight framelet filter bank reduces to the directional Haar tight framelet filter bank  
 206  $\text{DHF}_2 := \{a^H; b_1, \dots, b_6\}$  in [21, (3.5)].

207 For  $d = 3$ , it is a 3D directional Haar tight framelet filter bank  $\text{DHF}_3^1 := \{a^H; b_1, \dots, b_{28}\}$  with  
 208  $a^H = \frac{1}{8}(\delta_{(0,0,0)} + \delta_{(0,0,1)} + \delta_{(0,1,0)} + \delta_{(0,1,1)} + \delta_{(1,0,0)} + \delta_{(1,0,1)} + \delta_{(1,1,0)} + \delta_{(1,1,1)})$  and the 28  
 209 filters  $b_\iota = \frac{1}{8}(\delta_{\gamma_1^\iota} - \delta_{\gamma_2^\iota})$  for  $\iota = 1, \dots, 28$ . Since we employ the UDFmT (undecimated discrete  
 210 framelet transforms) for the  $W_{3D}$  in our model (1.5), only the partition of unity condition is needed  
 211 ( $\omega = 0$  in (2.1)) to guarantee the perfect reconstruction property. Hence, by considering filters with the  
 212 same direction, the 28 high-pass filters in  $\text{DHF}_3^1$  can be regrouped to 13 filters as a filter bank  $\text{DHF}_3^2$   
 213 with filters  $a^H, b_x, b_y, b_z, b_{xy}, b_{x,y}, b_{xz}, b_{x,z}, b_{yz}, b_{y,z}, b_{xyz}, b_{xy,z}, b_{x,y,z}, b_{xz,y}$  in [23]. Furthermore,  
 214 as demonstrated in [22], the output framelet coefficient sequences involving the  $z$ -filters, i.e., those  
 215  $b_z, b_{xz}, b_{xyz}$ , etc., are actually 'bad' features for our 3D signal reconstruction. They represent local  
 216 contrast discrepancy between coil images which do not play a role in our restriction process. Hence, in  
 217 [22], the filter bank  $\text{DHF}_3^2$  is further simplified to the filter bank  $\text{DHF}_3^3 := \{a^H; b_x, b_y, b_{xy}, b_{x,y}, b_{aux}\}$ ,  
 218 where  $b_x = \frac{1}{4}(\delta_{(1,0,0)} - \delta_{(0,0,0)})$ ,  $b_y = \frac{1}{4}(\delta_{(0,1,0)} - \delta_{(0,0,0)})$ ,  $b_{xy} = \frac{\sqrt{2}}{8}(\delta_{(1,1,0)} - \delta_{(0,0,0)})$ ,  $b_{x,y} =$   
 219  $\frac{\sqrt{2}}{8}(\delta_{(1,0,0)} - \delta_{(0,1,0)})$ , and the filter  $b_{aux}$  is determined by  $\widehat{b_{aux}} := 1 - (|\widehat{a^H}|^2 + |\widehat{b_x}|^2 + |\widehat{b_y}|^2 + |\widehat{b_{x,y}}|^2 +$   
 220  $|\widehat{b_{xy}}|^2)$ .

221 The 3D directional Haar filter bank  $\text{DHF}_3^3$  nicely fits into our SENSE pMRI regularization and  
 222 reconstruction with the following properties: (a) the lowpass filter  $a^H$  produces an underlying image  
 223 with harmonic pixel intensity for further process by the directional highpass filters; (b) the directional  
 224 highpass filters  $b_x, b_y, b_{xy}, b_{x,y}$  are properly chosen to capture the edge information for the sparse  
 225 representation, which facilitates the successful recovery in the  $\ell_1$ -based optimization models; (c) the  
 226 auxiliary filter  $b_{aux}$  guarantees the perfect reconstruction of the 3D filter bank and the UDFmT, where  
 227 in practice it does not participate in the shrinkage operation so that the procedure of UDFmTs is  
 228 equivalent to the UDFmT using the tight framelet filter bank  $\text{DHF}_3^2$ . We refer to [22, 23] for the  
 229 detailed construction of the  $\text{DHF}_3^3$  and the implementation of the UDFmT based on the  $\text{DHF}_3^3$ .

230 **3. Optimization models and the SENSE3d-algorithm.** The problem (1.1) is highly ill-  
 231 posed, because different pairs of  $u$  and  $s_\ell$  can bring about the same  $g_\ell$ . Under the priori knowledge  
 232 about  $u$  and  $s_\ell$ , our goal is to approximate the desired image  $u$  when  $s_\ell$  are unknown and the acquired  
 233  $K$ -space signal  $g_\ell$  are incomplete. To achieve this goal, we introduce a so-called SENSE3d-algorithm  
 234 for finding an estimate of both  $u$  and  $s_\ell$ . The basic steps for the SENSE3d-algorithm are outlined in  
 Algorithm 3.1.

---

**Algorithm 3.1** The SENSE3d-Algorithm

---

- 1: Given the observed  $K$ -space signal  $g_\ell$ , sampling matrix  $P$  and an initial sensitivity matrices  $s_\ell^0$ ,  
 $\ell = 1, 2, \dots, L$ .
  - 2: **for**  $k = 1, 2, \dots$  **do**
  - 3:   Slice-step: Find an estimate of  $u$  from the observed  $K$ -space signals  $g_\ell$  and the estimated  
 sensitivity matrices  $s_\ell$ ;
  - 4:   Sensitivity-step: Update the sensitivity vectors  $s_\ell$ , for  $\ell = 1, 2, \dots, L$ , from the observed  
 $K$ -space signal  $g_\ell$  and the estimated image  $u$ .
  - 5: **end for**
  - 6: Return  $u^\infty$  the estimate of the desired image  $u$ .
- 

235 The SENSE3d-algorithm is an iterative way to find the estimate of  $u$  by decoupling the effects  
 236 of  $u$  and the sensitivity maps  $s_\ell$ . We remark that a model called JSENSE that alternatively estimates  
 237 the slice image  $u$  and the sensitivity vectors  $s_\ell$  was proposed in [44] but it is without considering  
 238 any regularization technique and the convergence analysis. On the other hand, in the Slice-step of  
 239 Algorithm 3.1 for our SENSE3d model, we integrate in the regularization with the novel 3D direc-  
 240 tional Haar filter bank DHF<sub>3</sub> that captures the sparsity of the coils image. In the Sensitivity-step of  
 241 Algorithm 3.1, we propose a Tikhonov-type regularization that favors the smoothness of the sensi-  
 242 tivity mapping  $s_\ell$ ,  $\ell = 1, 2, \dots, L$ . For the regularized optimization problems in the Slice-step and  
 243 Sensitivity-step, we develop efficient algorithms to solve them and provide convergence analysis to  
 244 these algorithms.  
 245

**3.1. Slice-step: Object estimation.** We begin by introducing the basic notation. The pMRI  
 acquisition model involves complex numbers. For a vector  $u \in \mathbb{C}^n$ , we use  $\|u\|_2 := \sqrt{\sum_{j=1}^n |u[j]|^2}$ ,  
 $\|u\|_1 := \sum_{j=1}^n |u[j]|$ , and  $\|u\|_\infty := \max_{1 \leq j \leq n} |u[j]|$  to represent, respectively, the  $\ell_2$ -,  $\ell_1$ -, and  $\ell_\infty$ -  
 norm of  $u$ , where  $u[j]$  is the  $j$ th component of  $u$ . For a matrix  $A \in \mathbb{C}^{m \times n}$ , we define its norm as  
 follows:

$$\|A\|_2 := \max \{ \|Au\|_2 : u \in \mathbb{C}^n \text{ with } \|u\|_2 = 1 \}.$$

246 Hereafter,  $\text{Re}(\cdot)$  and  $\text{Im}(\cdot)$  stand for the real and imaginary parts, respectively. For  $u \in \mathbb{C}^n$ , we have  
 247  $u = \text{Re}(u) + i\text{Im}(u)$ , where both  $\text{Re}(u)$  and  $\text{Im}(u)$  are in  $\mathbb{R}^n$  and  $i$  is the imaginary unit satisfying  
 248  $i^2 = -1$ .

249 For the purpose of the exposition of optimization algorithms on  $\mathbb{C}^n$ , the inner product of two  
 250 vectors  $u$  and  $v$  in  $\mathbb{C}^n$  is defined as

$$(3.1) \quad \langle u, v \rangle := \text{Re}(u^\top v),$$

252 where  $u^\top$  is the conjugate transpose of  $u$ . With this inner product, the vector space  $\mathbb{C}^n$  is actually  
 253 viewed as the vector space  $\mathbb{R}^{2n}$ .

From the observed  $K$ -space signals  $g_\ell$  and the estimated sensitivity maps  $s_\ell$ , we propose to estimate  $u$  in (1.1) through an optimization model that is regularized by the prior knowledge of the coil images. Note that the  $\ell$ -th coil image  $s_\ell \odot u = \text{diag}(s_\ell)u = S_\ell u$ . From the identities  $S_\ell u = F^{-1}FS_\ell u$  and  $I_n = (I_n - P) + P$ , in the noise-free situation we have

$$S_\ell u = F^{-1}((I_n - P)FS_\ell u + PFS_\ell u) = F^{-1}(I_n - P)FS_\ell u + F^{-1}g_\ell$$

254 for all  $\ell = 1, 2, \dots, L$ . Putting all  $L$  coil images together, the above equations yield

$$255 \quad (3.2) \quad c = Nu + (I_L \otimes F^{-1})g,$$

256 where  $c = Su$  and  $N = (I_L \otimes (F^{-1}(I_n - P)F))S$ . Here,  $S$  is defined in (1.2) and  $\otimes$  denotes the  
257 *Kronecker product*. Equation (3.2) says that the integration of the coil images  $c$  is composed of the  
258 missing information  $Nu$  and the available information  $(I_L \otimes F^{-1})g$ .

259 Denoting  $W := W_{3D}$  the transformation matrix associated with the filter bank  $\text{DHF}_3^3$  onto the coil  
260 images  $c$ , we have  $Wc = W(Nu + (I_L \otimes F^{-1})g)$ . Using this identity, (1.3), and (3.2), we propose to  
261 estimate image  $u$  through the following optimization problem

$$262 \quad (3.3) \quad \min \left\{ \frac{1}{2} \|Mu - g\|_2^2 + \|\Gamma W(Nu + (I_L \otimes F^{-1})g)\|_1 : u \in \mathbb{R}^n \right\},$$

263 where  $\Gamma$  is a diagonal matrix with non-negative diagonal entries. In the objective function of (3.3), the  
264 term  $\frac{1}{2} \|Mu - g\|_2^2$  measures the faithfulness of the recovered image to the given data while the term  
265  $\|\Gamma W(Nu + (I_L \otimes F^{-1})g)\|_1$  relates to the sparsity of the coil images  $Nu + (I_L \otimes F^{-1})g$  under  $W$ .  
266 Note that the ideal image  $u$  is restricted in  $\mathbb{R}^n$ .

267 With the above preparation, we first present the PD3O (primal-dual three-operator) algorithm for  
268 solving (3.3) and the convergence analysis of the sequence generated by the algorithm. We postpone  
269 the discussion on the development and the convergence analysis of the algorithm in the Appendix 6.1  
270 to avoid a lengthy digression.

This algorithm is written as follows: given the initial guess  $(v^0, z^0) \in \mathbb{C}^n \times \mathbb{C}^d$  and the parameters  $\gamma, \delta$  and  $\Gamma$ , iterate

$$\begin{cases} u^k &= \text{Re}(v^k) \\ w^k &= (I - \gamma\delta AA^\top)z^k + \delta A(\bar{v}^k - \gamma M^\top(Mu^k - g)) \\ z^{k+1} &= (w^k + \delta b) - \text{soft}(w^k + \delta b, \Gamma) \\ v^{k+1} &= u^k - \gamma M^\top(Mu^k - g) - \gamma A^\top z^{k+1}. \end{cases}$$

Here,  $A = WN$ ,  $b = W(I_L \otimes F^{-1})g$  and  $w^k$  is the auxiliary variable. Furthermore,  $\text{soft}$  is the well-known soft shrinkage operator, i.e., for  $w \in \mathbb{C}^d$ ,

$$(\text{soft}(w, \Gamma))[j] = \max\{|w[j]| - \Gamma[j, j], 0\} \frac{w[j]}{|w[j]|}$$

271 for  $j = 1, 2, \dots, d$ . One iteration of the above scheme can be viewed as the operator  $T_{\text{PD3O}}$  (see  
272 (6.3a)–(6.3c) in Appendix 6.1 for its definition) such that  $(v^{k+1}, z^{k+1}) = T_{\text{PD3O}}(v^k, z^k)$ .

273 The theorem for the convergence analysis of the PD3O algorithm for problem (3.3) is given as  
274 follows.

275 **Theorem 3.1.** *Let the pair  $(v^*, z^*)$  be any fixed point of the  $\mathbb{T}_{\text{PD3O}}$  operator. Let  $\kappa$  be defined by*

$$276 \quad (3.4) \quad \kappa = \max_j \sum_{\ell=1}^L |s_\ell[j]|^2$$

and let  $\{v^k, z^k\}_{k \geq 0}$  be the sequence generated by the PD3O algorithm (6.3a)–(6.3c) with

$$(v^{k+1}, z^{k+1}) = \mathbb{T}_{\text{PD3O}}(v^k, z^k)$$

277 and the initial guess  $(v^0, z^0)$ . Choose  $\gamma$  and  $\delta$  such that  $\gamma < 2/\kappa$  and  $\gamma\delta < 1/\kappa$ . Define  $B :=$   
278  $\frac{\gamma}{\delta}(I - \gamma\delta AA^\top)$  and  $\|(v, z)\|_B := \sqrt{\|v\|^2 + \langle z, Bz \rangle}$ . Then, the following statements hold.

279 (i) The sequence  $\{\|(v^k, z^k) - (v^*, z^*)\|_B\}_{k \geq 0}$  is monotonically nonincreasing.

280 (ii) The sequence  $\{\|(v^{k+1}, z^{k+1}) - (v^k, z^k)\|_B\}_{k \geq 0}$  is monotonically nonincreasing. Moreover,  
281 we have  $\|(v^{k+1}, z^{k+1}) - (v^k, z^k)\|_B = o\left(\frac{1}{k+1}\right)$ .

282 The detailed proof of the above theorem is given in Appendix 6.1. We next focus on the estimation  
283 of the sensitivity maps  $s_\ell$ .

284 **3.2. Sensitivity-step: Sensitivity maps estimation.** Once we have an approximation to  
285 the target image  $u$ , we can use it to update the sensitivity maps  $s_\ell$ ,  $\ell = 1, 2, \dots, L$ . From the acquisi-  
286 tion model (1.1) and the facts that  $I_n = P + (I_n - P)$  and  $g_\ell = PF(s_\ell \odot u)$  in the noise-free case,  
287 the approximation of the full  $K$ -space signal, denoted by  $g_{est,\ell}$  and received by the  $\ell$ th coil, can be  
288 modeled as

$$289 \quad (3.5) \quad g_{est,\ell} = g_\ell + (I_n - P)F(s_\ell \odot u).$$

290 That is,  $g_{est,\ell}$  is composed of the observed partial  $K$ -space information  $g_\ell$  and the estimated unobserv-  
291 able  $K$ -space data  $(I - P)F(s_\ell \odot u)$ . In the noise-free case, due to  $s_\ell \odot u = u \odot s_\ell = \text{diag}(u)s_\ell$ , we  
292 indeed have

$$293 \quad (3.6) \quad g_{est,\ell} = F(s_\ell \odot u) = (F \text{diag}(u))s_\ell.$$

294 Define

$$295 \quad (3.7) \quad g_{est} = \begin{bmatrix} g_{est,1} \\ \vdots \\ g_{est,L} \end{bmatrix}, Q = I_L \otimes (F \text{diag}(u)), s = \begin{bmatrix} s_1 \\ \vdots \\ s_L \end{bmatrix}.$$

296 Here,  $g_{est} \in \mathbb{C}^{Ln}$ ,  $Q \in \mathbb{C}^{Ln \times Ln}$ , and  $s \in \mathbb{C}^{Ln}$ . With these preparations, a compact representation of  
297 (3.6) is as follows:

$$298 \quad (3.8) \quad g_{est} = Qs.$$

299 To estimate a faithful  $s$  from model (3.8), we should take both reliable  $K$ -space data information  
300 from  $g_{est}$  and prior knowledge on  $s$  into consideration. Regarding the prior knowledge on  $s$ , each  
301 sensitivity map  $s_\ell$  is assumed to be smooth and the energy of the values coming from the same location  
302 of the sensitivity maps is identical and equals to one, that is,  $\sum_{\ell=1}^L |s_\ell[j]|^2 = 1$ , for all  $j = 1, \dots, n$ ,

303 see [24]. Due to  $u \odot s_\ell = (hs_\ell) \odot (u/h)$  holds for any nonzero constant  $h$ , the constraint on the  
 304 sensitivity maps  $s_\ell$  ensures the uniqueness of the underlying problem. Therefore, we define the domain

$$305 \quad (3.9) \quad D := \{s : s \in \mathbb{C}^{Ln}, \sum_{\ell=1}^L |s[j + (\ell - 1)n]|^2 = 1 \text{ for } j = 1, \dots, n\}.$$

306 With these preparations, our proposed optimization problem for estimating  $s$  from model (3.8) has a  
 307 form of

$$308 \quad (3.10) \quad \min \left\{ \frac{1}{2} \|P_{sel}(Qs - g_{est})\|_2^2 + \frac{1}{2} \|\Gamma_s Ws\|_2^2 : s \in D \right\},$$

309 where  $P_{sel}$  is a sampling matrix and  $W = W_{3D}$  is associated with the 3D directional Haar framelet  
 310 transform used in the Slice-step. Here  $\Gamma_s$  is a diagonal matrix whose diagonal entries corresponding  
 311 to the framelet coefficients from lowpass filter of the framelet system are zero and the others have the  
 312 same value. The use of  $P_{sel}$  here is twofold. First, the  $K$ -space data is usually fully sampled near  
 313 its center, i.e., the ACS lines, and thus gives more accurate estimation of  $g_{est}$  near the center. The  
 314 sampling matrix  $P_{sel}$  is hence defined to sample coefficients near the center of  $K$ -space only. Second,  
 315 the smooth assumption on each  $s_\ell$  implies that the frequency response of  $s_\ell$  is concentrated around  
 316 the center of the  $K$ -space (a low-passed signal). Therefore, there is no need to use the full  $K$ -space  
 317 data. Moreover,  $P_{sel}$  reduces the computation cost significantly. In our experiments,  $P_{sel}$  is indeed the  
 318 sampling matrix corresponding to the ACS line.

319 Since the objective function of the optimization problem (3.10) is Lipschitz continuous, problem  
 320 (3.10) can be solved through the forward-backward algorithm (see, for example, [1]). It reads as, for  
 321 any initial guess  $s^0$ , iterate

$$322 \quad (3.11) \quad s^{k+1} = \text{proj}_D(s^k - \tau_k(Q^\top P_{sel}(Qs^k - g_{est}) + W^\top \Gamma^2 Ws^k)),$$

where  $\tau_k > 0$ . Here, if  $t = \text{proj}_D(s)$  for  $s \in \mathbb{C}^{Ln}$ , then for each  $j = 1, 2, \dots, n$ , let  $\tilde{t} = [t[j], t[j +$   
 $n], \dots, t[j + (L - 1)n]]$  and  $\tilde{s} = [s[k], s[k + n], \dots, s[k + (L - 1)n]]$ , we have

$$\tilde{t} = \begin{cases} \frac{\tilde{s}}{\|\tilde{s}\|_2}, & \text{if } \|\tilde{s}\|_2 \neq 0; \\ \text{any unit-vector in } \mathbb{C}^L, & \text{otherwise.} \end{cases}$$

323 The convergence analysis of the iterative scheme (3.11) is given in the following theorem.

**Theorem 3.2.** *Given an  $\epsilon \in \left(0, \frac{1}{2(\|u\|_\infty^2 + \|\text{diag}(\Gamma)\|_\infty^2)}\right)$  and a sequence of stepsize  $\tau_k$  such that  
 $\epsilon < \tau_k < \frac{1}{\|u\|_\infty^2 + \|\text{diag}(\Gamma)\|_\infty^2} - \epsilon$ , we consider the sequence  $\{s^k\}_{k \geq 0}$  generated by (3.11). Then the  
 sequence converges to a point  $s^*$  in  $D$  such that*

$$Q^\top P_{sel}(Qs^* - g_{est}) + Q^\top \Gamma^2 Qs^* + \nu \text{diag}(I_L \otimes \nu)s^* = 0$$

324 for some vector  $\nu \in \mathbb{R}^n$  with positive  $\nu_i \geq 0$ ,  $i = 1, 2, \dots, n$ .

325 The proof of the above theorem is given in Appendix 6.2.

326 **4. Experiments.** In this section, we provide numerical experiments to demonstrate the perfor-  
 327 mance of our *SENSE3d* model. We begin by reviewing some related work on SENSE and GRAPPA.  
 328 We then provide numerical experiments for the comparisons of our model with some traditional meth-  
 329 ods as well as some deep learning methods.

330 **4.1. Related work.** For the SENSE method, total variation (TV) is one of the regularization  
 331 techniques that has an ability to recover the edge details in the target image for the pMRI problem [43].  
 332 It is well known that TV does not distinguish between jumps and smooth transitions, and tends to give  
 333 piecewise constant images with staircase artifacts. Total generalized variation (TGV) with high-order  
 334 differential operator can remove the staircase artifacts caused by TV, and the TGV of second-order  
 335 is applied to parallel imaging in [17]. Wavelet transforms are adopted to detect artifacts appeared  
 336 in the basic SENSE reconstruction and reduce the artifacts by emphasizing the sparse representation  
 337 of the underlying image [4]. However, the reconstructed image will suffer from ringing artifacts  
 338 when the wavelet coefficients are modified in an incorrect way. The 2D directional Haar framelet  
 339 (DHF) based regularization technique assimilating the advantages of both total variation and wavelet  
 340 regularization, called FADHFA, was proposed for SENSE to preserve details of slice and remove noise  
 341 in [21]. To adaptively represent the image with sparse canonical coefficients by tight frame, a data-  
 342 driven tight frame based off-the-grid regularization model was proposed for the compressive sensing  
 343 MRI reconstruction in [3]. The non-convex and non-smooth Euler’s elastica functional was proposed  
 344 to regularize SENSE reconstruction in [42]. These 2D regularization techniques only focus on each  
 345 coil image independently, and the redundant information among multi-coil images of pMRI are not  
 346 considered in the SENSE reconstructions.

347 The generalized autocalibrating partially parallel acquisitions (GRAPPA) in [9] is a  $K$ -space me-  
 348 thod and interpolates the missing data in the  $K$ -space for each coil from the multi-coil neighbouring  
 349  $K$ -space samples. The GRAPPA method can reconstruct almost the same quality of images as those  
 350 from the SENSE method [2], but it requires the ACS data, near the center of  $K$ -space, to estimate  
 351 the interpolation weights or coil sensitivities. In [37], sparsity-promoting calibration was proposed  
 352 to regularize the GRAPPA-based interpolation weights for reconstructing high quality MRI images.  
 353 By exploiting the nonlinear relationship between ACS and missing data, a kernel-based approach was  
 354 suggested to interpolate the missing data in the  $K$ -space [25]. Iterative self-consistent parallel imaging  
 355 reconstruction (SPIRiT) extends the GRAPPA’s interpolation weights on sampled and unsampled data  
 356 and fills missing  $K$ -space as an inverse problem [24]. ESPIRiT is a “soft” SENSE reconstruction using  
 357 the eigenvectors of a calibration matrix constructed by the SPIRiT model as sensitivity maps, and is  
 358 called  $\ell_1$ -ESPIRiT by regularizing the wavelet coefficients of the target images with  $\ell_1$  norm [33].  
 359 Joint sparsity of the wavelet coefficients of each coil image at same position is applied to SPIRiT  
 360 model ( $\ell_1$ -SPIRiT) [27] and SENSE model (JSCSENSE) [5] to further improve the quality of the  
 361 reconstruction results. Since ESPIRiT does not consider the phase of image, an algorithm called  
 362 VCC-ESPIRiT [34] incorporating the virtual conjugate coils was proposed to estimate the sensitivity  
 363 maps that include the absolute phase of the image. A 3D directional Haar tight framelet (3DHF) was  
 364 proposed to regularize the related features between coil images reconstructed by SPIRiT model for  
 365 reducing the aliasing artifacts caused by the downsampling operation [23].

366 The filling of  $K$ -space data was formulated as the low-rank matrix completion problem in [14].  
 367 The low-rank matrix modeling of local  $K$ -space neighborhoods (LORAKS) [10], and simultaneous  
 368 autocalibration and  $K$ -space estimation (SAKE) [31] use local neighborhoods of multi-coil  $K$ -space

369 data to construct low-rank matrices for regularizing parallel imaging reconstruction. Under smooth  
 370 phase assumptions, the LORAKS method also imposes phase constraints on low-rank matrices. When  
 371 an image is with the finite rate of innovation, then its  $K$ -space data has a property with low-ranked  
 372 weighted Hankel structured matrix, leading to an annihilating filter-based low rank Hankel matrix  
 373 approach (ALOHA) [15]. Jointing sparsity of the patches from multi-coil images using sparse dictio-  
 374 nary was proposed to regularize the reconstruction coil MR images by considering the cross-channel  
 375 relationships in [36].

376 Deep learning methods based on many neural network architectures can discover the internal rela-  
 377 tionship of large-scale data through training and learning, and make multi-level abstract representation  
 378 of data [40, 41]. A deep convolutional neural network was proposed to learn regularization part of  
 379 the optimization model for inverse problem and applied to the pMRI problem in [16]. U-Net is a  
 380 commonly used neural network model in medical image processing [30], and has been successfully  
 381 applied to MRI reconstruction [32, 45]. An end-to-end variation network (VarNet) [32] is a more pow-  
 382 erful model built upon the fastMRI-UNet model [45]. The VarNet model utilizes a sensitivity map  
 383 estimation module, a refinement module, and a data consistency module to estimate missing  $K$ -space  
 384 data and reconstruct MRI images. It achieves good results on the fastMRI dataset and served as the  
 385 baseline model for the 2020 fastMRI challenge [26].

386 Deep learning methods for pMRI reconstruction require large number of multi-coil  $K$ -space data  
 387 and accurate information about the MR machine acquisitions, however, the parameters of the imaging  
 388 setting of MRI machine (for example, field of view, slice thicknesses, and others) maybe different for  
 389 different cases. For example, a person’s heartbeat, slight body jitter and other factors in the process  
 390 of scanning can form gradient information similar to adversarial attack, which affects the accuracy  
 391 of prediction and results in blurred anatomical structure details and artifacts in reconstructed MRI  
 392 images using deep learning methods [8]. Hence, in this paper, we focus on approaches without the  
 393 needs of large scale data but simply with the few given multi-coil data in the pMRI reconstruction.  
 394 Nevertheless, we provide comparisons of our methods with the deep learning methods as well.

395 **4.2. Parameter settings.** The parameter setting of our *SENSE3d*-algorithm is as follow. In  
 396 the Slice-step, the parameters  $\gamma = 1.99$ ,  $\delta = 0.5$ , and for a more precise choice of  $\Gamma$ , the thresholding  
 397 parameter, we refer to [22, Section 4.2]; In the Sensitivity-step, all nonzero diagonal entries of the  
 398 diagonal matrix  $\Gamma$  are identical, say each  $s$ -th diagonal entry  $\lambda_s = 0.05$  for all experiments. After  
 399 this parameter is determined, we choose  $\tau_k = \frac{0.99}{2(\|u\|_\infty^2 + \lambda_s^2)}$  and 25 iterations for Sensitivity-step. We  
 400 terminate our method when  $\|u^{k+1} - u^k\|_2 / \|u^k\|_2 < 10^{-6}$  or when the number of iterations exceeds  
 401 40. Here  $u^k$  is the  $k$ th iteration produced by the underlying algorithm. Our *SENSE3d*-algorithm only  
 402 updates the sensitivity maps at  $k = 8, 16$  and  $24$  by the Sensitivity-step, and then fixes them after  
 403  $k = 24$  to guarantee convergence in Slice-step. The two-level decomposition of  $\text{DHF}_3^3$  is adopted in  
 404 all experiments.

405 Several state-of-the-art methods reviewed above, including the fast adaptive DHF algorithm FAD-  
 406 HFA [21], the  $\ell_1$ -ESPIRiT method [33], and ALOHA [15], are adopted to further compare with our  
 407 *SENSE3d* model in numerical experiments. The source code of the  $\ell_1$ -ESPIRiT method was down-  
 408 loaded from the website of Michael Lustig<sup>1</sup>, and its default settings are used except for kernel size  
 409 with  $5 \times 5$ , maximal iteration 50 and regularization parameter  $\lambda$  set by hand for its best performance.

---

<sup>1</sup>The code is available at: <http://people.eecs.berkeley.edu/~mlustig/Software.html>

410 The source code of ALOHA method is available at this website of BISPL<sup>2</sup>, and its default settings are  
 411 used except for the follows: pyramidal decomposition with decreasing LMaFit tolerances, annihilating  
 412 filters, and smoothed regularization parameter named as *sroi*.

413 To evaluate the performance of the algorithms for removing artifacts and preserving details, we  
 414 use the HaarPSI index to calculate the similarity between the reference image and the reconstructed  
 415 image [29]<sup>3</sup>. The HaarPSI index ranges from 0 to 1, and higher value means that the algorithm is  
 416 better to reconstruct details of slice and remove artifacts.

417 The experiments will be carried out on the real phantom and in-vivo data to test different pMRI  
 418 reconstruction algorithms. The phantom MR images are acquired on a 3T MRI System (Tim Trio,  
 419 Siemens, Erlangen, Germany). A turbo spin-echo sequence was used to acquire  $T_2$ -weighted images.  
 420 The detailed imaging parameters are as follows: field of view (FOV) =  $256 \times 256$  mm<sup>2</sup>, image matrix  
 421 size =  $512 \times 512$ , slice thicknesses (ST) = 3 mm, flip angle = 180 degree, repetition time (TR) = 4000  
 422 ms, echo time (TE) = 71 ms, echo train length (ETL) = 11 and number of excitation (NEX) = 1.

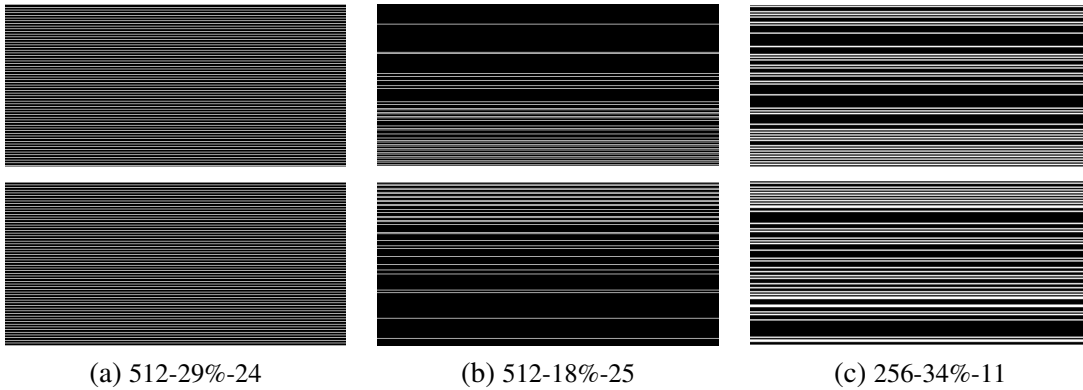


**Figure 3.** Sampling modes for the  $K$ -space. (a) 29% data by the uniform sampling model of  $512 \times 512$  (one line taken from every four lines) with 24 ACS lines (the middle white area); (b) 18% data by the random sampling model of  $512 \times 512$  with 25 ACS lines; (c) 34% data by the random sampling model of  $256 \times 256$  with 11 ACS lines.

423 **4.3. Comparisons with other methods: MRI phantoms.** In this subsection, three pMRI  
 424 reconstruction methods FADHFA [21],  $\ell_1$ -ESPIRiT [33] and ALOHA [15] are compared with our  
 425 proposed *SENSE3d* model on the two slices of the MRI phantoms.

426 We first use four MRI phantom images under the  $512 \times 512$  (512-29%-24) sampling model as  
 427 shown in Fig. 3(a). That is, the uniform sampling model of  $512 \times 512$  with one line taken from every  
 428 four lines and with 24 ACS lines. In Fig. 4, the part (a) is the SoS image reconstructed from the full  $K$ -  
 429 space data, while the part (b) is the SoS image with blurring and aliasing artifacts by four coil images  
 430 from the downsampled  $K$ -space data by the uniform sampling mode in Fig. 3(a). The regularization  
 431 parameter  $\lambda$  is to be 0.035 and 0.001 for  $\ell_1$ -ESPIRiT and our *SENSE3d* model, respectively. The  
 432 settings for ALOHA are four levels of pyramidal decomposition with decreasing LMaFit tolerances  
 433 (0.3, 0.03, 0.003, 0.0003), annihilating filters with size of  $11 \times 11$ , and *sroi* = 10.

434 The four pMRI reconstruction algorithms can retrieve most of the information from the parts of

<sup>2</sup>The code is available at: <https://bispl.weebly.com/aloha-for-mr-recon.html>

<sup>3</sup>The code is available at: <http://www.math.uni-bremen.de/cda/HaarPSI/>

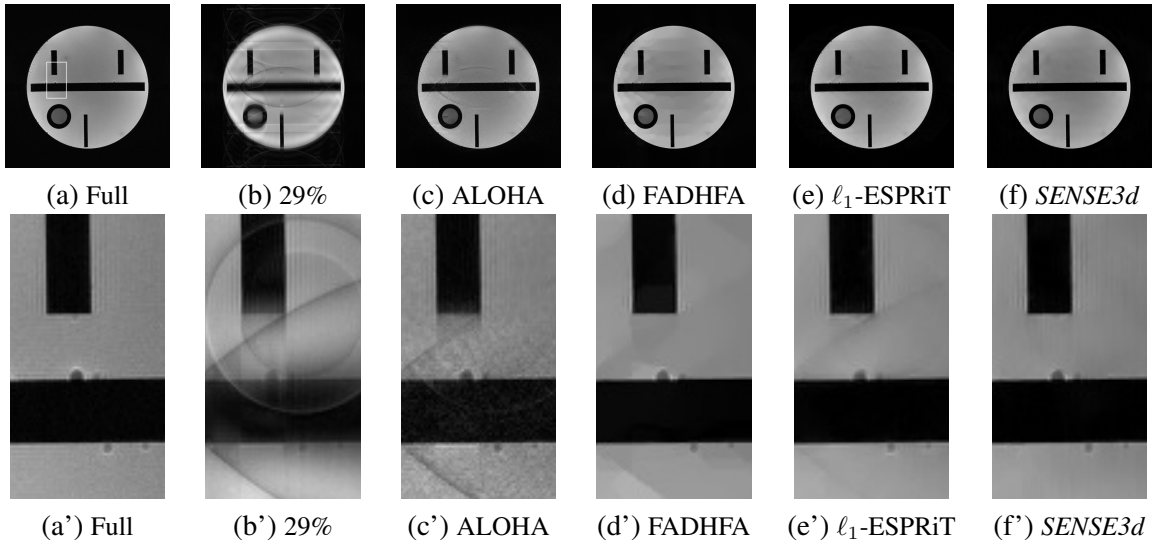


**Figure 4.** MRI Phantoms of Slice 1 with size 512-by-512. (a) Reference SoS image by four full  $K$ -space data with zoom-in area. (b) SoS image by four coil images by 29%  $K$ -space data on uniform sampling mode in Figure 3(a). (c) ALOHA. (d) FADHFA. (e)  $\ell_1$ -ESPIRiT. (f) Our proposed 3D-US model. (a')–(f') are the zoom-in parts of (a)–(f), respectively.

435 the  $K$ -space data, but the images in Figs. 4(c), (d) and (e) by ALOHA, FADHFA and  $\ell_1$ -ESPIRiT  
 436 respectively, have some obvious aliasing artifacts, which are removed by our  $SENSE3d$  model and  
 437 do not appear in Fig. 4(f). That is to say, the correlated features by 3D tight framelet can be utilized  
 438 to regularize the reconstruction image. We provide the zoom-in parts of the reconstructed images in  
 439 Figs. 4(a')–(f') for distinguishing their difference. One can see that the ‘circle’ and ‘line’ false aliasing  
 440 artifacts in (b') are mostly reduced by the regularized algorithms, but false ‘circle’ structures on the  
 441 black region and and noisy artifacts still appear in the zoom-in image (c') by low-rank regularization,  
 442 while the ‘line’ artifact exists at the left-down corner of the zoom-in image (d') by 2D-U model and  
 443 at the middle of the zoom-in image (e') by  $\ell_1$ -ESPIRiT using 2D wavelet regularization without con-  
 444 sidering the correlated features of coil images. The Fig. 4(f') by our  $SENSE3d$  model does not have  
 445 these aliasing artifacts and it removes noise and preserves details of the edges more closer to the refer-  
 446 ence image (a') with full  $K$ -space data. The HaarPSI indexes in Table 1 of these four zoom-in images  
 447 by ALOHA, FADHFA,  $\ell_1$ -ESPIRiT, and  $SENSE3d$  are 0.68, 0.81, 0.84 and 0.90, respectively. Our  
 448  $SENSE3d$  algorithm can get the highest index, which means that our  $SENSE3d$  model can efficiently  
 449 remove artifacts and preserve details.

450 We next use four MRI phantom images under the  $512 \times 512$  (512-18%-25) sampling model as  
 451 shown in Fig. 3(b). That is, we use 18% sampling rate and 25 ACS lines to collect  $K$ -space data for this  
 452 phantom slice. The parameter settings for ALOHA are four levels of pyramidal decomposition with  
 453 decreasing LMaFit tolerances (0.3, 0.03, 0.003, 0.0003),  $9 \times 9$  annihilating filters, and  $sroi = 8$ . The  
 454 reconstructed results by ALOHA, FADHFA,  $\ell_1$ -ESPIRiT with regularization parameter  $\lambda = 0.025$   
 455 and the proposed  $SENSE3d$  model with parameter  $\lambda = 0.0002$  are shown in Figs. 5(c), (d), (e) and (f),  
 456 respectively.

457 Due to the downsampling operation on the  $K$ -space, the SoS image in Fig. 5(b) from 18%  $K$ -space  
 458 data is blurry and has lots of aliasing artifacts. The ALOHA, FADHFA,  $\ell_1$ -ESPIRiT and proposed

Table 1

The HaarPSI indexes of the zoom-in parts of reconstructed images by ALOHA, FADHFA,  $\ell_1$ -ESPIRiT, and SENSE3d in Algorithm 3.1 for removing artifacts and preserving details.

Algorithm	ALOHA	FADHFA	$\ell_1$ -ESPIRiT	SENSE3d
Zoom-in parts in Figures				
Fig. 4	0.68	0.81	0.84	<b>0.90</b>
Fig. 5	0.73	0.85	0.86	<b>0.92</b>
Fig. 7				
First row	0.89	0.93	0.95	<b>0.96</b>
Second row	0.87	0.90	0.93	<b>0.96</b>

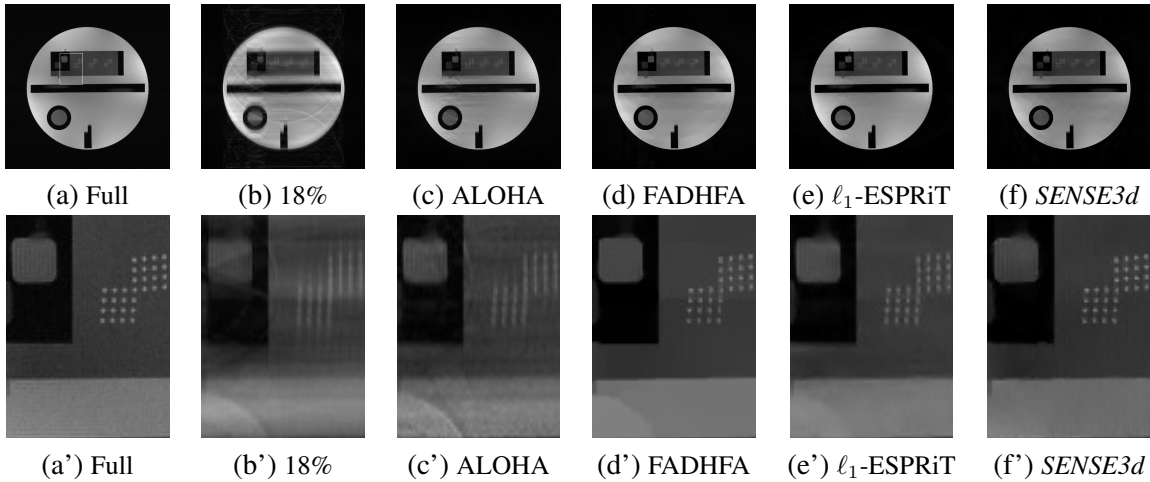


**Figure 5.** MRI Phantoms of Slice 2 with size 512-by-512. (a) Reference SoS image by four full  $K$ -space data, (b) SoS image by 18%  $K$ -space data with sampling model in Figure 3(b). (c) ALOHA. (d) FADHFA. (e)  $\ell_1$ -ESPIRiT. (f) Our proposed SENSE3d model. (a')–(f') are the Zoom-in parts of (a)–(f), respectively.

459 SENSE3d model can reconstruct most of details of the target slice and reduce aliasing with respect to  
 460 reference image by full  $K$ -space data in Figs. 5(c)–(f). However, the Fig. 5(c) by the ALOHA method  
 461 has obvious aliasing artifacts and false structures, which is not suitable for doctor’s diagnosis. We  
 462 present the zoom-in parts of the reconstruction images into Figs. 5(a')–(f') to further compare these  
 463 methods. It is obvious to see that our SENSE3d model can efficiently remove aliasing artifacts and  
 464 keep the structures of the imaging slice. The ALOHA method is not efficient to preserve the shape of  
 465 the bright ‘points’ and separate boundary between the upper and lower regions, and aliasing artifacts  
 466 in the zoom-in images in Fig. 5(c'); The  $\ell_1$ -ESPIRiT is better than ALOHA to retrieve the bright  
 467 ‘points’ and reduce aliasing artifacts, but it is worse than the FADHFA and our SENSE3d model to  
 468 preserve the boundary edges; The FADHFA is almost the same as the SENSE3d to preserve structure  
 469 details of the slice, but the Fig. 5(d') by FADHFA has ‘arc’ artifacts at left-down of the zoom-in image  
 470 and false ‘gray’ edges covering the regions of bright ‘points’. The Fig. 5(e') by  $\ell_1$ -ESPIRiT also has  
 471 the aliasing artifact problem as that in Fig. 5(d') by FADHFA, but it is not efficient to preserve sharp  
 472 edges and blurs these region. All the above issues in Figs. 5(c')–(e') do not appear in Fig. 5(f') by our  
 473 SENSE3d model. The HaarPSI indexes in Table 1 of these four zoom-in images by ALOHA, FADHFA

474 ,  $\ell_1$ -ESPRiT, and *SENSE3d* are 0.73, 0.85, 0.86 and 0.92, respectively. It shows that our *SENSE3d*  
 475 model gives the best performance for reconstructing the slice image.

476 The 3D tight framelet regularization is essentially different from the 2D tight framelet regulariza-  
 477 tion when extracting the features of the correlated coil images for pMRI reconstruction. Our *SENSE3d*  
 478 model not only has merit of 2D tight framelet-based FADHFA to preserve details but also utilizes cor-  
 479 related features to remove aliasing artifacts caused by downsampling operation in  $K$ -space. This case  
 480 again shows our *SENSE3d* pMRI reconstruction algorithm can reconstruct most details of the slice and  
 481 remove aliasing artifacts when the accelerated sampling rate is high.

482 **4.4. Comparisons with other methods: In-vivo data.** In this subsection we test our  
 483 *SENSE3d* model on MRI data that are obtained by head examination from a healthy volunteer. The  
 484 detailed imaging was done on a 3T MRI system. Transverse  $T_2$ -weighted images were acquired with  
 485 a turbo spin-echo sequence. The detail imaging parameters are as follows: field of view =  $256 \times 256$   
 486  $\text{mm}^2$ , image matrix size =  $256 \times 256$ , slice thicknesses = 3 mm, flip angle = 150 degree, repetition  
 487 time = 5920 ms, echo time = 101 ms, echo train length = 11 and number of excitation = 1.

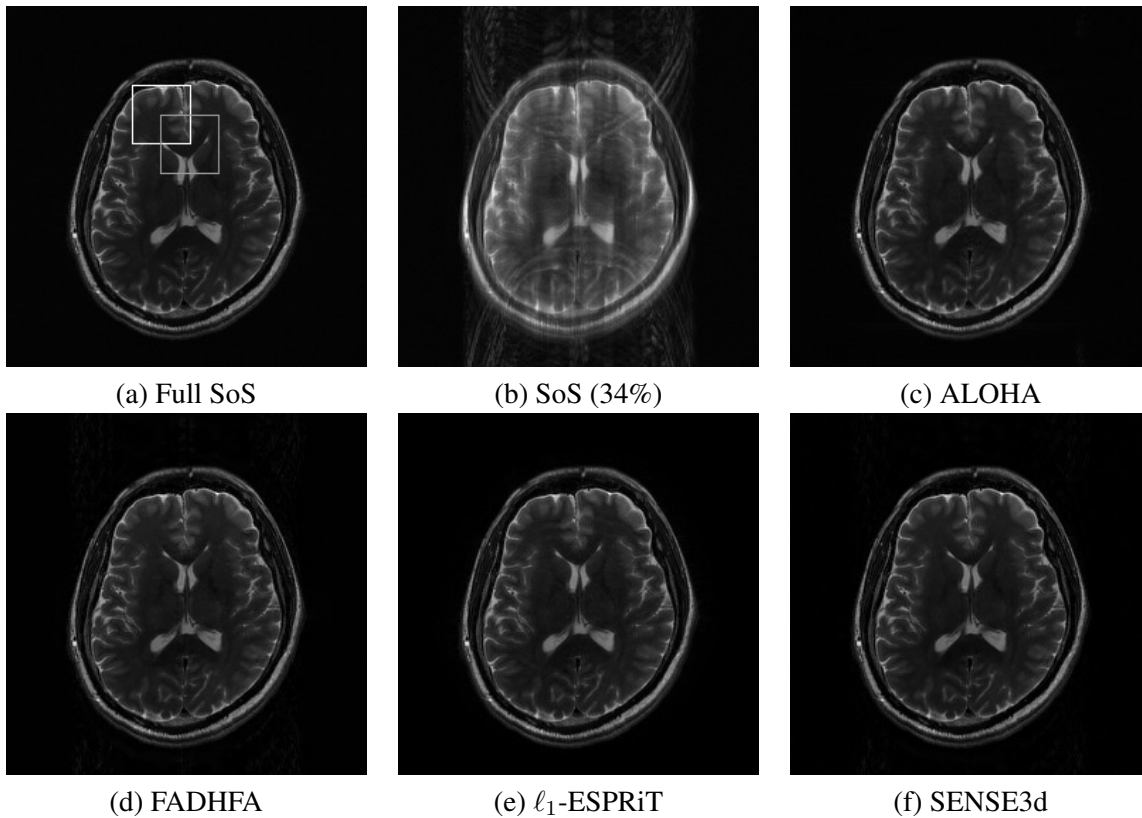


**Figure 6.** In-vivo data with sampling model  $256 \times 256$  (256-34%-11) as shown in Fig. 3(c) with two to-be zoom-in square areas. (a) Reference SoS image of 32 coil images by full  $K$ -space data with two zoom-in regions. (b) SoS image by 34%  $K$ -space data. (c) ALOHA. (d) FADHFA. (e)  $\ell_1$ -ESPRiT. (f) Our *SENSE3d* model.

488 The magnetic resonance signal of each slice is received by 32 channels, and the reference image of  
 489 one slice in Fig. 6(a) is a SoS image of 32 coil images by full of the  $K$ -space data. In phase direction,

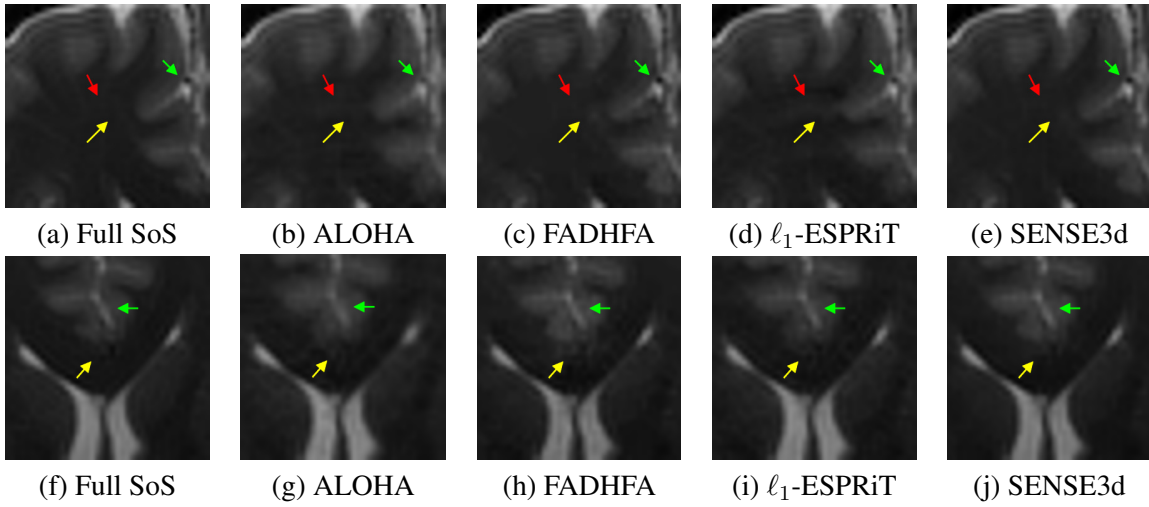


**Figure 7.** Two zoom-in parts of Fig. 6. (a)(f) Reference SoS image. (b)(g) ALOHA. (c)(h) FADHFA. (d)(i)  $\ell_1$ -ESPRiT. (e)(j) Our SENSE3d model.

490 about 34%  $K$ -space data are collected using the pseudo-random sampling mode with 11 ACS lines in  
 491 Fig. 3(c). The resulting SoS image of the collected 34%  $K$ -space data in Fig. 6(b) is noisy and the brain  
 492 structures are blurry. Furthermore, faint semicircle-like aliasing artifacts can be seen in the upper and  
 493 lower portions of the image due to the accelerating  $K$ -space sampling mode.

494 The reconstructions by the ALOHA, FADHFA,  $\ell_1$ -ESPRiT and our *SENSE3d* model are shown  
 495 in Figs. 6(c), (d), (e) and (f), respectively. Their parameter settings are as follows: four levels of pyra-  
 496 midal decomposition with decreasing LMaFit tolerances ( $10^{-1}$ ,  $10^{-2}$ ,  $10^{-3}$ ,  $10^{-4}$ ),  $9 \times 9$  annihilating  
 497 filters, and regularization parameter  $sroi = 1.1$  for ALOHA;  $\ell_1$ -ESPRiT with  $\lambda = 0.003$  and our 3D  
 498 *SENSE3d*-Algorithm with  $\lambda = 0.00001$ . Clearly, the quality of the images in Figs. 6(c), (d), (e) and  
 499 (f) are much better than the one in Fig. 6(b) in terms of the structures of the slice, the levels of noise  
 500 and the aliasing artifacts.

501 To discriminate the difference of reconstructed images, we zoom-in two square regions as in  
 502 Fig. 6(a) to compare the quality of the reconstructions by ALOHA, FADHFA,  $\ell_1$ -ESPRiT and our  
 503 *SENSE3d* model. The first region at the left side of frontal lobe is zoomed-in and provided in  
 504 Figs. 7(a)–(e). According to HaarPSI indexes in Table 1, the Figs. 7(b)–(e) by ALOHA, FADHFA  
 505 ,  $\ell_1$ -ESPRiT, and *SENSE3d* are 0.89, 0.93, 0.95 and 0.96, respectively. Our *SENSE3d* algorithm is  
 506 the best to reconstruct slice details from in-vivo data.

507 We label three positions by red, green and yellow arrows to compare their differences by different  
 508 algorithms. The artery pointed by green arrow in Fig. 7(b) by ALOHA is not clear and blurred, but  
 509 structures of artery in Figs. 7(c), (d), and (e) respectively by FADHFA,  $\ell_1$ -ESPRiT and *SENSE3d*  
 510 are more obvious than that by ALOHA. The FADHFA and *SENSE3d* models are better than the  $\ell_1$ -  
 511 ESPRiT method, which reconstruct the structures of artery almost same as reference one in Fig. 7(a).  
 512 At the region of white matter between red arrow and yellow arrow, there are aliasing artifacts in  
 513 Fig. 7(d) by  $\ell_1$ -ESPRiT, extending from the frontal lobe into white matter; the boundary between the  
 514 frontal lobe and white matter is blurry in Fig. 7(b) by ALOHA; there are ‘white artifact’ (yellow arrow  
 515 pointing) in Fig. 7(b) by FADHFA; but Fig. 7(e) by our *SENSE3d* model doesn’t have these aliasing

516 problems and provides obvious boundary between tissues, and is very close to reference image in  
 517 Fig. 7(a).

518 We zoom-in another part of slice at the anterior border of the corpus callosum region, and present  
 519 zoom-in images in Figs. 7(f)–(j). The lobus (green arrow pointing) in Figs. 7(h), (i) and (j), respectively  
 520 reconstructed by FADHFA,  $\ell_1$ -ESPIRiT and our *SENSE3d*, still have better tissue structure than that in  
 521 Fig. 7(g) by ALOHA. The low-rank regularized method ALOHA doesn't preserve details in the tissue.  
 522 The yellow arrow pointing regions in Figs. 7(g), (h) and (i), respectively reconstructed by ALOHA,  
 523 FADHFA,  $\ell_1$ -ESPIRiT have aliasing artifacts at the anterior border of corpus callosum, which are false  
 524 structures and do not appear in the reference image in Fig. 7(f). However, in Fig. 7(j), the aliasing  
 525 artifacts is removed by our *SENSE3d* model and the geometry structures of the border is retrieved  
 526 almost the same as the reference one. The HaarPSI indexes in Table 1, the Figs. 7(f)–(i) by ALOHA,  
 527 FADHFA,  $\ell_1$ -ESPIRiT, and *SENSE3d* are 0.87, 0.90, 0.93 and 0.96, respectively. The highest HaarPSI  
 528 index of our *SENSE3d* algorithm is consistent with our visual observation. The ALOHA, FADHFA  
 529 and  $\ell_1$ -ESPIRiT methods are not very efficient to remove these artifact appeared in Fig. 6(b), but our  
 530 *SENSE3d* model can be efficient to remove these aliasing artifacts and its reconstructed structures of  
 531 tissues is close to reference image in Fig. 6(a). That is to say, 3D tight framelet-based *SENSE3d*-  
 532 algorithm has a greater capacity of preserving edges and reducing most of the aliasing artifacts caused  
 533 by downsampling operation in  $K$ -space than the 2D tight framelet-based, 2D wavelet-based and low-  
 534 rank based regularization algorithms.

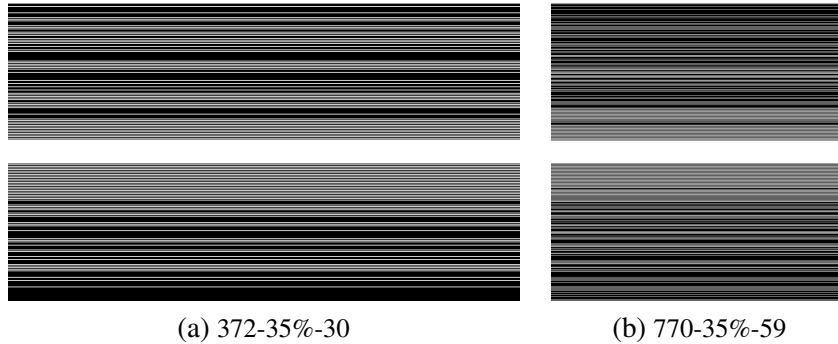


**Figure 8.** Sampling modes for the  $K$ -space. (a) 35% data by the uniform sampling model of  $372 \times 640$  with 30 ACS lines ; (b) 35% data by the random sampling model of  $770 \times 768$  with 59 ACS lines.

535 **4.5. Comparisons with deep learning methods: Knee data.** In this section, we compare  
 536 our *SENSE3d* model with deep learning model VarNet [32]<sup>4</sup> that is built upon the fastMRI-UNet  
 537 model [45] with fastMRI dataset.<sup>5</sup>

538 A set of knee with full  $K$ -space data from the fastMRI dataset is used for this section. This knee  
 539 dataset is acquired using a clinical 1.5T system with a 2D turbo spin-echo sequence and a conventional  
 540 Cartesian 2D TSE protocol. The detailed imaging parameters are as follows: field of view =  $280.00 \times$   
 541  $162.82 \times 4.50$  mm<sup>3</sup>, image matrix size =  $640 \times 372$ , slice thicknesses = 4.5 mm, flip angle = 140

<sup>4</sup>The code is available at: [https://github.com/facebookresearch/fastMRI/tree/main/fastmri\\_examples/varnet](https://github.com/facebookresearch/fastMRI/tree/main/fastmri_examples/varnet)

<sup>5</sup>The dataset is available at: <http://fastmri.med.nyu.edu/> and served as the baseline model for the 2020 fastMRI challenge [26].

542 degree, repetition time = 2800 ms, echo time = 32 ms and echo train length = 4. The VarNet crops  
 543 the reconstructed images from the network outputs with size  $640 \times 372$  to be image blocks with size  
 544  $320 \times 320$  centered on the original ones. We follow the settings of the VarNet model. The fully  
 545 sampled images and reconstructed images by *SENSE3d* are also taken out from the same region for  
 546 comparisons. Note that this knee dataset serves as a *validation set* for the VarNet model in training  
 547 process. Hence, it is no doubt that the trained model VarNet gives superior performance on such data  
 548 than the fastMRI-UNet model.

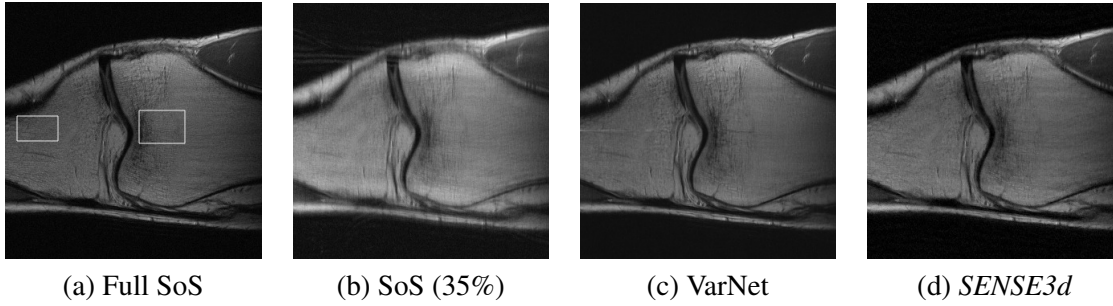


**Figure 9.** *FastMRI* data with sampling model 372-35%-30 as shown in Fig. 8(a) with two to-be zoom-in rectangle areas. (a) Reference SoS image of 15 coil images by full  $K$ -space data with two zoom-in regions. (b) SoS image by 35%  $K$ -space data. (c) VarNet. (d) Our *SENSE3d* model.

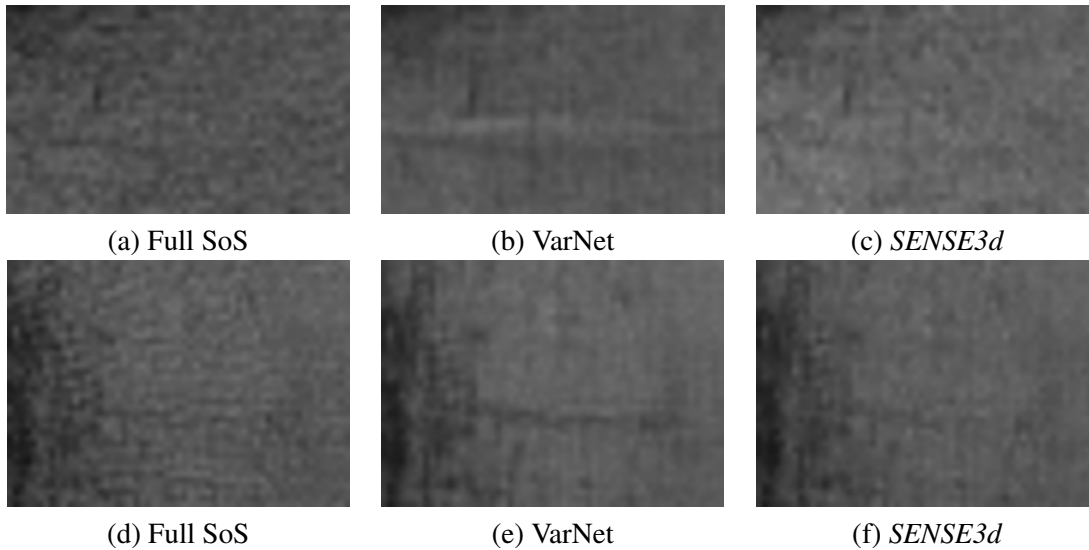


**Figure 10.** Two zoom-in parts of Fig. 9. (a)(d) Reference SoS image. (b)(e) VarNet. (c)(f) Our *SENSE3d* model.

549 The reference image in Fig. 9(a) is a SoS image by 15 coil images with full  $K$ -space data. In phase  
 550 direction, about 35%  $K$ -space data are collected using the pseudo-random sampling mode with 30 ACS  
 551 lines in Fig. 8(a). The resulting SoS image of the collected 35%  $K$ -space data in Fig. 9(b) is noisy and  
 552 the knee structures are blurry. Furthermore, numerous faint elongated aliasing artifacts can be seen  
 553 across the entire image due to the accelerating  $K$ -space sampling mode. The reconstructions by the

554 VarNet and our *SENSE3d* model are shown in Figs. 9(c) and (d), respectively. The parameter setting  
 555 of our 3D *SENSE3d*-algorithm is  $\lambda = 0.0005$ , which remains the same throughout the subsequent  
 556 experiments. Clearly, the quality of the images in Figs. 9(c) and (d) are much better than the one in  
 557 Fig. 9(b) in terms of the structures of the slice, the levels of noise and the aliasing artifacts. To compare  
 558 the difference between these two reconstructed images, we zoom-in parts of the femur and tibia regions  
 559 and show them in Fig. 10. It is obvious that the zoom-in images by the VarNet are smoother than the  
 560 original ones (lost of details) and have some aliasing artifacts, tibia image with ‘white line’ and femur  
 561 image with ‘black line’. But our *SENSE3d* algorithm can suppress these artifacts and its reconstructed  
 562 images are with closer structures to the reference one. We provide their HaarPSI index for further  
 563 comparisons. The HaarPSI index provided in Table 2 for tibia and femur images in Figs. 10(c) and (f)  
 564 by our *SENSE3d* are 0.891 and 0.894, respectively. But the HaarPSI index by the VarNet in Figs. 10(b)  
 565 and (e) are 0.866 and 0.879, respectively. Our *SENSE3d* gets higher HaarPSI index than that by the  
 566 VarNet.

**Table 2**

*The HaarPSI indexes of the zoom-in parts of reconstructed images by VarNet, fastMRI-UNet, and SENSE3d in Algorithm 3.1 for removing artifacts and preserving details.*

Algorithm	Fig. 10		Algorithm	Fig. 12	
	First row	Second row		First row	Second row
VarNet	0.866	0.879	fastMRI-UNet	0.906	0.836
<i>SENSE3d</i>	<b>0.891</b>	<b>0.894</b>	<i>SENSE3d</i>	<b>0.970</b>	<b>0.961</b>

567 Another knee dataset is different from the data used in FastMRI, which is provided at this MRI  
 568 data website <sup>6</sup>. This knee dataset is acquired using a clinical 2.89T system with a turbo spin-echo  
 569 sequence. The detail imaging parameters are as follows: field of view =  $280 \times 280.7 \times 4.5$  mm<sup>3</sup>,  
 570 image matrix size =  $768 \times 770$ , slice thicknesses = 4.5 mm, flip angle = 150 degree, repetition time =  
 571 2800 ms, echo time = 22 ms.

572 We attempt to use the VarNet to reconstruct the MRI image on this new knee data. However, the  
 573 VarNet cannot produce correct result on this new knee data. The main reason is due to the inaccurate  
 574 sensitivity maps estimated by the VarNet besides the common generalization limitation of the network  
 575 model such as inconsistent image from the fastMRI dataset, different machines data acquisition set-  
 576 tings, and so on. We hence use another model, the fastMRI-UNet [45], that has less restrictions, to  
 577 reconstruct the result and compare it with our model. Unlike the VarNet, the fastMRI-UNet directly  
 578 takes  $K$ -space data as input and produces reconstructed MRI images, without the need for a sensitivity  
 579 map estimation model. The source code of fastMRI-UNet is available at the GitHub website<sup>7</sup>.

580 We use the sampling mode with 59 ACS lines in Fig. 8(b) to collect 35%  $K$ -space for the fastMRI-  
 581 UNet and our *SENSE3d* to reconstruct the target image. The reconstructions by the fastMRI-UNet  
 582 and our *SENSE3d* model are shown in Fig. 11(c) and (d) respectively. The SoS image in Fig. 11(b)  
 583 by the collected 35%  $K$ -space data is blurry, but reconstructed images by the fastMRI-UNet and our  
 584 *SENSE3d* model are clear with more structure details. To compare the difference between Fig. 11(c)  
 585 and (d), we zoom-in parts of the popliteus and Soleus muscle regions and show them in Figure 10. The  
 586 reconstructed images by our *SENSE3d* model are with clear organizational details than the images by

<sup>6</sup><http://www.mridata.org>

<sup>7</sup>The code is available at: [https://github.com/facebookresearch/fastMRI/tree/main/fastmri\\_examples/unet](https://github.com/facebookresearch/fastMRI/tree/main/fastmri_examples/unet)

587 the fastMRI-UNet. The popliteus part by our model is almost close to reference one with HaarPSI  
 588 value 0.961 (see Table 2), but the image by the fastMRI-UNet is only 0.836. HaarPSI value of another  
 589 part at soleus muscle by the fastMRI-UNet and our SENSE3d model are 0.906 and 0.970, respectively.  
 590 Our model gives 0.064 higher than the fastMRI-UNet model. This case shows that our model is stable  
 591 to reconstruct image and get nice results from the different data by different machine acquisition.

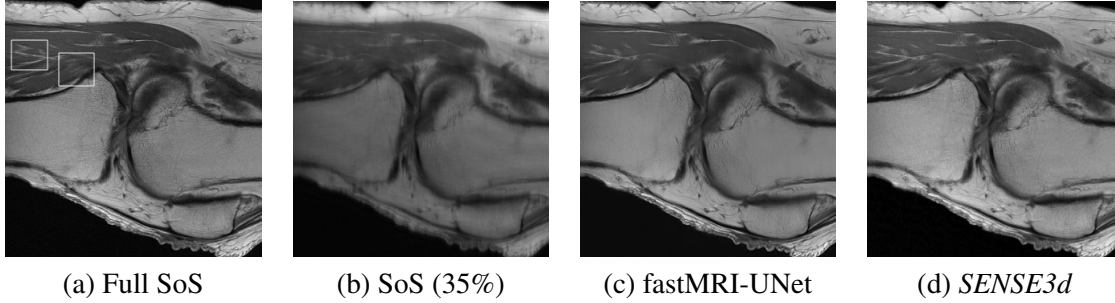


**Figure 11.** MRI data with sampling model 770-35%-59 as shown in Fig. 8(b) with two to-be zoom-in rectangle areas. (a) Reference SoS image of 15 coil images by full  $K$ -space data with two zoom-in regions. (b) SoS image by 35%  $K$ -space data. (c) fastMRI-UNet. (d) Our SENSE3d model.

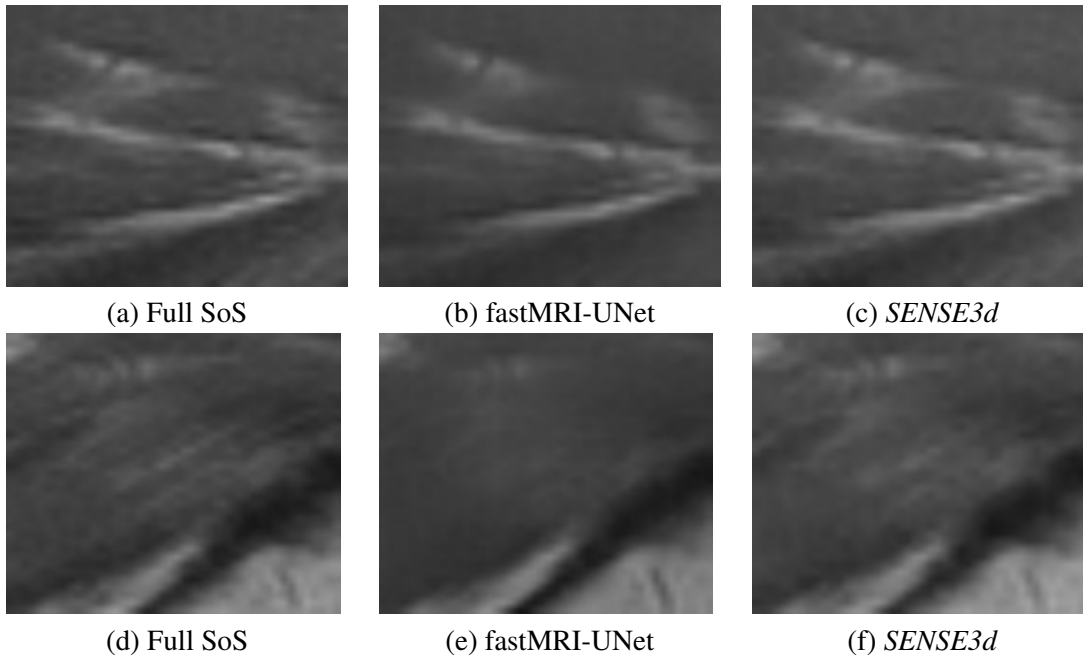


**Figure 12.** Two zoom-in parts of Fig. 11. (a)(d) Reference SoS image. (b)(e) fastMRI-UNet. (c)(f) SENSE3d.

592 **5. Conclusions and further remarks.** We have proposed an effective *SENSE3d* model for  
 593 the pMRI reconstruction. The proposed method can reconstruct high quality images from the sampled  
 594  $K$ -space data with a high acceleration rate by decoupling effects of the desired image (slice) and  
 595 sensitivity maps. The developed *SENSE3d*-algorithm, which consists of a sequence of alternating

596 Slice-step and Sensitivity-step, exploits the decoupled slices and sensitivity maps. Each Slice-step  
 597 solves a convex optimization problem for an estimated image with the given estimations of sensitivity  
 598 maps while each Sensitivity-step solves a non-convex optimization problem for estimated sensitivity  
 599 maps with the given estimation of the desired image. The convergence analysis for the optimization  
 600 algorithm in both Slice-step and Sensitivity-step has been studied. Numerical results on various data  
 601 and comparisons to other state-of-the-art methods including deep learning methods have demonstrated  
 602 that the proposed method can produce images of high quality and reduce aliasing artifacts efficiently  
 603 caused by inaccurate estimation of each coil sensitivity.

604 The using of neural networks is to learn the relationship between input data ( $K$ -space data) and  
 605 output data (for example, slice images) by training data. Thus, the databases with a large number of  
 606 multi-coil  $K$ -space data are needed to train the neural networks for pMRI reconstruction [18]. The  
 607 challenge of pMRI reconstruction by using neural networks is their instability of predicting output  
 608 data when the imaging conditions of input data are different with different training conditions [35].  
 609 How to take the advantages of our model to improve the performance of the models based on deep  
 610 learning methods can be one of our future research topics.

## 611 6. Appendix.

612 **6.1. Proof of Theorem 3.1.** In this appendix, we give the proof of Theorem 3.1. To this end,  
 we first introduce our notation and recall some necessary background materials from optimization.  
 The class of all lower semicontinuous convex functions  $f : \mathbb{C}^d \rightarrow (-\infty, +\infty]$  such that  $\text{dom } f :=$   
 $\{x \in \mathbb{C}^d : f(x) < +\infty\} \neq \emptyset$  is denoted by  $\Gamma_0(\mathbb{C}^d)$ . The indicator function of a closed convex set  $C$   
 in  $\mathbb{C}^d$  is defined, at  $u \in \mathbb{C}^d$ , as

$$\iota_C(u) := \begin{cases} 0, & \text{if } u \in C, \\ +\infty, & \text{otherwise.} \end{cases}$$

612 Clearly, the indicator function  $\iota_C$  is in  $\Gamma_0(\mathbb{C}^d)$  for any closed nonempty convex set  $C$ .

For a function  $f \in \Gamma_0(\mathbb{C}^d)$ , the proximity operator of  $f$  with parameter  $\lambda$ , denoted by  $\text{prox}_{\lambda f}$ , is  
 a mapping from  $\mathbb{C}^d$  to itself, defined for a given point  $x \in \mathbb{C}^d$  by

$$\text{prox}_{\lambda f}(x) := \operatorname{argmin} \left\{ \frac{1}{2} \|u - x\|_2^2 + \lambda f(u) : u \in \mathbb{C}^d \right\}.$$

613 We also need the notation of conjugate. The conjugate of  $f \in \Gamma_0(\mathbb{C}^d)$  is the function  $f^* \in \Gamma_0(\mathbb{C}^d)$   
 614 defined at  $x \in \mathbb{C}^d$  by  $f^*(x) := \sup\{\langle u, x \rangle - f(u) : u \in \mathbb{C}^d\}$ . A key property of the proximity  
 615 operators of  $f$  and its conjugate is

$$616 \quad (6.1) \quad \text{prox}_{\lambda f}(x) + \lambda \text{prox}_{\lambda^{-1} f^*}(x/\lambda) = x,$$

617 which holds for all  $x \in \mathbb{C}^n$  and any  $\lambda > 0$ .

For a real function  $f$  defined on  $\mathbb{C}^d$ , we say  $f$  is Fréchet differentiable at  $x \in \mathbb{C}^d$  if there exists a  
 $v \in \mathbb{C}^d$  such that

$$\lim_{y \rightarrow x} \frac{|f(y) - f(x) - \langle v, y - x \rangle|}{\|y - x\|_2} = 0.$$

618 The vector  $v$  is called the gradient of  $f$  at  $x$ , denoted by  $\nabla f(x)$ . As an example,  $\nabla(\|A \cdot -b\|_2^2) =$   
 619  $A^\top(A \cdot -b)$ , where  $A \in \mathbb{C}^{d \times n}$  and  $b \in \mathbb{C}^d$ .

620 We consider the following optimization problem

$$621 \quad (6.2) \quad \min_{x \in \mathbb{C}^n} p(x) + q(x) + r(Ax),$$

622 where  $A$  is a  $d \times n$  matrix,  $p \in \Gamma_0(\mathbb{C}^n)$  is differentiable,  $q \in \Gamma_0(\mathbb{C}^n)$ , and  $r \in \Gamma_0(\mathbb{C}^d)$ .

623 Several algorithms have been developed for the optimization problem (6.2), see, for example,  
624 [20, 39]. We adopt the algorithm given in [39] for problem (6.2) since it converges under a weaker  
625 condition and can choose a larger step-size, yielding a faster convergence. This algorithm, named as  
626 Primal-Dual Three-Operator splitting (PD3O), has the following iteration:

$$627 \quad (6.3a) \quad x^k = \text{prox}_{\gamma q}(y^k)$$

$$628 \quad (6.3b) \quad z^{k+1} = \text{prox}_{\delta r^*}((I - \gamma \delta A A^\top)z^k + \delta A(2x^k - y^k - \gamma \nabla p(x^k)))$$

$$629 \quad (6.3c) \quad y^{k+1} = x^k - \gamma \nabla p(x^k) - \gamma A^\top z^{k+1}$$

631 One PD3O iteration can be viewed as an operator  $T_{\text{PD3O}}$  such that  $(y^{k+1}, z^{k+1}) = T_{\text{PD3O}}(y^k, z^k)$ .  
632 The convergence analysis of PD3O is given in the following lemma.

633 **Lemma 6.1 (Sublinear convergence rate [39]).** *Let  $p \in \Gamma_0(\mathbb{C}^n)$  and its gradient be Lipschitz  
634 continuous with constant  $\nu$ . Choose  $\gamma$  and  $\delta$  such that  $\gamma < 2/\nu$  and  $B = \frac{\gamma}{\delta}(I - \gamma \delta A A^\top)$  is positive  
635 definite. Let  $(y^*, z^*)$  be any fixed point of  $T_{\text{PD3O}}$ , and  $\{(y^k, z^k)\}_{k \geq 0}$  be the sequence generated by  
636 PD3O. Define  $\|(y, z)\|_B := \sqrt{\|y\|^2 + \langle z, Bz \rangle}$ . Then, the following statements hold.*

637 (i) *The sequence  $\{(\|(y^k, z^k) - (y^*, z^*)\|_B)\}_{k \geq 0}$  is monotonically nonincreasing.*

638 (ii) *The sequence  $\{(\|(y^{k+1}, z^{k+1}) - (y^k, z^k)\|_B)\}_{k \geq 0}$  is monotonically nonincreasing. Moreover,*

$$\|(y^{k+1}, z^{k+1}) - (y^k, z^k)\|_B^2 = o\left(\frac{1}{k+1}\right).$$

639 We remark that the statements in Lemma 6.1 are originally presented in real vector space  $\mathbb{R}^n$  (see [39]).  
640 By using the inner product (3.1) for  $\mathbb{C}^n$ , we essentially work with real vector space  $\mathbb{R}^{2n}$ . Therefore,  
641 the results in Lemma 6.1 hold on  $\mathbb{C}^n$  as well.

642 By identifying  $p, q, r$  and  $A$  in (6.2), respectively, as follows

$$643 \quad (6.4) \quad p(\cdot) = \frac{1}{2}\|M \cdot -g\|^2, \quad q(\cdot) = \iota_{\mathbb{R}^n}(\cdot), \quad r(\cdot) = \|\Gamma(\cdot + b)\|_1, \quad A = WN$$

644 with  $b = W(I_L \otimes F^{-1})g$ , the PD3O algorithm can be applied for solving problem (3.3). To efficiently  
645 implement this algorithm, we need to know both  $\text{prox}_q$  and  $\text{prox}_{\delta r^*}$ . By the definition of proximity  
646 operator,  $\text{prox}_q = \text{Re}$ , i.e.,  $\text{prox}_q$  takes the real part of an input. The proximity operator  $\text{prox}_{\delta r^*}$  is  
647 given in the next lemma.

648 **Lemma 6.2.** *Let  $r$  be given in (6.4). Then, for  $\delta > 0$  and  $z \in \mathbb{C}^d$ ,  $\text{prox}_{\delta r^*}(z) = (z + \delta b) -$   
 $\text{prox}_{\|\Gamma(\cdot)\|_1}(z + \delta b)$ .*

649 *Proof.* Write  $w = \text{prox}_{\delta r^*}(z)$ . From the identity (6.1),  $w = z - \delta \text{prox}_{\delta^{-1}r}(\delta^{-1}z)$ . Based on  
650 the separable property of  $r$  in (6.4), that is,  $r(u) = \|\Gamma(u + b)\|_1 = \sum_{k=1}^d \gamma[k]|u[k] + b[k]|$ , we have  
651 that  $w[k] = z[k] - \delta \text{prox}_{\delta^{-1}\gamma[k]| \cdot + b[k]|}(\delta^{-1}z[k])$ , for  $k = 1, 2, \dots, d$ . By a simple manipulation on  
652 the above proximity operator, we have that  $w[k] = (z[k] + \delta b[k]) - \text{prox}_{\gamma[k]| \cdot |}(z[k] + \delta b[k])$ . This  
653 completes the proof of this result. ■

654 The proximity operator  $\text{prox}_{\|\cdot\|_{\Gamma, \|\cdot\|_1}}$  is the well-known soft shrinkage operator  $\text{soft}(x, \Gamma)$ . To show the  
 655 convergence of the PD3O algorithm under the proper choices of parameters  $\gamma$  and  $\delta$ , we need the  
 656 following lemma.

657 **Lemma 6.3.** *Let  $M$  and  $g$  be given in (1.2), and let  $p$  and  $A$  be given in (6.4). Then, the following*  
 658 *statements hold:*

659 (i). *The gradient of  $p$  is  $\kappa$ -Lipschitz continuous, where  $\kappa$  is given in (3.4).*

660 (ii). *For any positive numbers  $\gamma$  and  $\delta$ , the matrix  $I - \gamma\delta AA^\top$  is positive definite if and only if  $\gamma\delta < 1/\kappa$ .*

661 *Proof.* Item (i): Note that  $\nabla p(u) = M^\top(Mu - g)$ . Then,  $\nabla p$  is  $\|M\|^2$ -Lipschitz continuous.  
 662 Define  $Q = \sum_{\ell=1}^L s_\ell s_\ell^\top$  which is the entry-wise conjugate of the matrix  $\sum_{\ell=1}^L s_\ell s_\ell^\top$ . From (1.2), we  
 663 have  $M^\top M = \sum_{\ell=1}^L \text{diag}(\bar{s}_\ell) F^\top P F S_\ell = (F^\top P F) \odot Q$ . Since  $Q$  is positive semi-definite matrix, we  
 664 have, for example, by Theorem 5.5.18 in [13], that  $\|M^\top M\|_2 \leq \max_{i,j} |Q[i,j]| \|F^\top P F\|_2$ . Further,  
 665 due to  $\|F^\top P F\| \leq 1$ ,  $\max_{i,j} |Q[i,j]| = \max_k |Q[k,k]|$ , and  $Q[k,k] = \sum_{\ell=1}^L |s_\ell[k]|^2$ , we have  
 666  $\|M^\top M\|_2 \leq \kappa$ .

667 Item (ii): The proof relies on the estimation of the norm of  $AA^\top$ . From  $A = WN$  and  $W^\top W =$   
 668  $I$ , one has  $\|AA^\top\|_2 = \|A^\top A\|_2 = \|N^\top N\|_2$ . Similar to the discussion in Item (i), we have  $N^\top N =$   
 669  $(F^\top(I - P)F) \odot Q$  and  $\|N^\top N\|_2 \leq \kappa$ . Therefore, the largest eigenvalue of  $AA^\top$  is less than  $\kappa$ . As  
 670 a result,  $I - \gamma\delta AA^\top$  is positive definite if and only if  $\gamma\delta < 1/\kappa$ . This completes the proof. ■

671 *Proof.* (Theorem 3.1) By Lemma 6.3, the gradient  $p$  in (6.4) is  $\kappa$ -Lipschitz continuous and the  
 672 matrix  $B$  is positive definite if and only if  $\gamma\delta < 1/\kappa$ , the result of this theorem follows immediately  
 673 from Lemma 6.1. ■

674 **6.2. Proof of Theorem 3.2.** For given  $P_{sel}$ ,  $M$ ,  $g_{est}$ ,  $\Gamma$  and  $W$  in (3.10), define

$$675 \quad (6.5) \quad h(s) := \frac{1}{2} \|P_{sel}(Qs - g_{est})\|_2^2 + \frac{1}{2} \|\Gamma W s\|_2^2.$$

676 We have the following result for the function  $h$ .

677 **Lemma 6.4.** *Let  $h$  be defined in (6.5). Then, the gradient of  $h$  is Lipschitz continuous with*  
 678 *Lipschitz constant  $\|u\|_\infty^2 + \|\text{diag}(\Gamma)\|_\infty^2$ .*

679 *Proof.* Note that  $\nabla h(s) = Q^\top P_{sel}(Qs - g_{est}) + W^\top \Gamma^2 W s$ . For any vectors  $s_1$  and  $s_2$ , we have  
 680  $\|\nabla h(s_1) - \nabla h(s_2)\|_2 = \|(Q^\top P_{sel}Q + W^\top \Gamma^2 W)(s_1 - s_2)\|_2 \leq (\|Q\|_2^2 \|P_{sel}\|_2 + \|W\|_2^2 \|\Gamma\|_2^2) \|s_1 -$   
 681  $s_2\|_2$ . We know that  $\|P_{sel}\|_2 = 1$ ,  $\|W^\top\|_2 = 1$ , and  $\|\Gamma\|_2 = \|\text{diag}(\Gamma)\|_\infty$ . Next we estimate the norm  
 682 of  $Q$ . Since

$$683 \quad \begin{aligned} Q^\top Q &= (I_L \otimes (F \text{diag}(u)))^\top (I_L \otimes (F \text{diag}(u))) \\ 684 &= (I_L \otimes (\text{diag}(u) F^{-1})) (I_L \otimes (F \text{diag}(u))) \\ 685 &= I_L \otimes (\text{diag}(u) \text{diag}(u)), \end{aligned}$$

686 we have that  $\|Q\|_2^2 = \|Q^\top Q\|_2 = \|I_L \otimes (\text{diag}(u) \text{diag}(u))\|_2 = \|\text{diag}(u)\|_2^2 = \|u\|_\infty^2$ . Hence, the  
 687 gradient of  $h$  is Lipschitz continuous with Lipschitz constant  $\|u\|_\infty^2 + \|\text{diag}(\Gamma)\|_\infty^2$ . ■

688 *Proof.* (Theorem 3.2) Note that  $h(s)$  is a quadratic polynomial with respect to  $s$  and the set  $D$   
 689 given in (3.9) is determined by a set of polynomials. Then,  $h(s) + \iota_D(s)$  is a Kurdyka-Łojasiewicz  
 690 function (see, e.g., [1]). Hence, the result is the direct consequence of Theorem 5.3 of [1]. ■

691

## REFERENCES

- 692 [1] H. ATTOUCH, J. BOLTE, AND B. SVAITER, *Convergence of descent methods for semi-algebraic and tame prob-*  
693 *lems: proximal algorithms, forward-backward splitting, and regularized Gauss-Seidel methods*, *Mathematical*  
694 *Programming, Ser. A*, 137 (2013), pp. 91–129.
- 695 [2] M. BLAIMER, F. BREUER, M. MUELLER, R. M. HEIDEMANN, M. A. GRISWOLD, AND P. M. JAKOB, *SMASH,*  
696 *SENSE, PILS, GRAPPA: how to choose the optimal method*, *Topics in Magnetic Resonance Imaging*, 15 (2004),  
697 pp. 223–236.
- 698 [3] J.-F. CAI, J. K. CHOI, AND K. WEI, *Data driven tight frame for compressed sensing MRI reconstruction via off-the-*  
699 *grid regularization*, *SIAM Journal on Imaging Sciences*, 13 (2020), pp. 1272–1301.
- 700 [4] L. CHAÛRI, J. C. PESQUET, A. BENAZZA-BENYAHIA, AND P. CIUCIU, *A wavelet-based regularized reconstruc-*  
701 *tion algorithm for SENSE parallel MRI with applications to neuroimaging*, *Medical Image Analysis*, 12 (2011),  
702 pp. 185–201.
- 703 [5] I. Y. CHUN, B. ADCOCK, AND T. M. TALAVAGE, *Efficient compressed sensing SENSE pMRI reconstruction with*  
704 *joint sparsity promotion*, *IEEE Transactions on Medical Imaging*, 35 (2016), pp. 354–368.
- 705 [6] M. DONEVA, *Mathematical models for magnetic resonance imaging reconstruction: an overview of the approaches,*  
706 *problems, and future research areas*, *IEEE Signal Processing Magazine*, 37 (2020), pp. 24–32.
- 707 [7] W. A. EDELSTEIN, J. M. HUTCHISON, G. JOHNSON, AND T. REDPATH, *Spin warp NMR imaging and applications*  
708 *to human whole-body imaging*, *Physics in medicine & biology*, 25 (1980), p. 751.
- 709 [8] S. G. FINLAYSON, J. D. BOWERS, J. ITO, J. L. ZITTRAIN, A. L. BEAM, AND I. S. KOHANE, *Adversarial attacks*  
710 *on medical machine learning*, *Science*, 363 (2019), pp. 1287–1289.
- 711 [9] M. A. GRISWOLD, P. M. JAKOB, R. M. HEIDEMANN, M. NITTKA, V. JELLUS, J. WANG, B. KIEFER, AND  
712 A. HAASE, *Generalized autocalibrating partially parallel acquisitions (GRAPPA)*, *Magnetic Resonance in*  
713 *Medicine*, 47 (2002), pp. 1202–1210.
- 714 [10] J. P. HALDAR AND J. ZHUO, *P-LORAKS: low-rank modeling of local k-space neighborhoods with parallel imaging*  
715 *data*, *Magnetic Resonance in Medicine*, 75 (2016), pp. 1499–1514.
- 716 [11] B. HAN, *Framelets and Wavelets: Algorithms, Analysis, and Applications*, Springer International Publishing, 2018.
- 717 [12] B. HAN, T. LI, AND X. ZHUANG, *Directional compactly supported box spline tight framelets with simple geometric*  
718 *structure*, *Applied Mathematics Letters*, 91 (2019).
- 719 [13] R. HORN AND C. JOHNSON, *Topics in matrix analysis*, Cambridge University Press, 1991.
- 720 [14] M. JACOB, M. P. MANI, AND J. C. YE, *Structured low-rank algorithms: theory, magnetic resonance applications,*  
721 *and links to machine learning*, *IEEE Signal Processing Magazine*, 37 (2020), pp. 54–68.
- 722 [15] K. H. JIN, D. LEE, AND J. C. YE, *A general framework for compressed sensing and parallel MRI using annihilating*  
723 *filter based low-rank hankel matrix*, *IEEE Transactions on Computational Imaging*, 2 (2016), pp. 480–495.
- 724 [16] K. H. JIN, M. T. MCCANN, E. FROUSTEY, AND M. UNSER, *Deep convolutional neural network for inverse prob-*  
725 *lems in imaging*, *IEEE Transactions on Image Processing*, 26 (2017), pp. 4509–4522.
- 726 [17] F. KNOLL, C. CLASON, K. BREDIES, M. UECKER, AND R. STOLLBERGER, *Parallel imaging with nonlinear*  
727 *reconstruction using variational penalties*, *Magnetic Resonance in Medicine*, 67 (2012), pp. 34–41.
- 728 [18] F. KNOLL, K. HAMMERNIK, C. ZHANG, S. MOELLER, T. POCK, D. K. SODICKSON, AND M. AKCAKAYA, *Deep-*  
729 *learning methods for parallel magnetic resonance image reconstruction: a survey of the current approaches,*  
730 *trends, and issues*, *IEEE Signal Processing Magazine*, 37 (2020), pp. 128–140.
- 731 [19] J. LI, H. FENG, AND X. ZHUANG, *Convolutional neural networks for spherical signal processing via area-regular*  
732 *spherical haar tight framelets*, *IEEE Transactions on Neural Networks and Learning Systems*, (2022).
- 733 [20] Q. LI AND N. ZHANG, *Fast proximity-gradient algorithms for structured convex optimization problems*, *Applied and*  
734 *Computational Harmonic Analysis*, 41 (2016), pp. 491 – 517.
- 735 [21] Y.-R. LI, R. H. CHAN, L. SHEN, Y.-C. HSU, AND W.-Y. I. TSENG, *An adaptive directional haar framelet-based*  
736 *reconstruction algorithm for parallel magnetic resonance imaging*, *SIAM Journal on Imaging Sciences*, 9 (2016),  
737 pp. 794–821.
- 738 [22] Y.-R. LI, L. SHEN, AND X. ZHUANG, *A tailor-made 3-dimensional directional haar semi-tight framelet for pMRI*  
739 *reconstruction*, *Applied and Computational Harmonic Analysis*, 60 (2022), pp. 446–470.
- 740 [23] Y.-R. LI AND X. ZHUANG, *Parallel magnetic resonance imaging reconstruction algorithm by 3-dimension direc-*  
741 *tional Haar tight framelet regularization*, in *SPIE Proc.*, San Diego, 2019, pp. 111381C–1–8.
- 742 [24] M. LUSTIG AND J. M. PAULY, *SPIRiT: iterative self-consistent parallel imaging reconstruction from arbitrary k-*  
743 *space*, *Magnetic Resonance in Medicine*, 64 (2010), pp. 457–471.

- 744 [25] J. LYU, U. NAKARMI, D. LIANG, J. SHENG, AND L. YING, *Kernel-based nonlinear approach to parallel*  
745 *MRI reconstruction*, IEEE Transactions on Medical Imaging, 38 (2019), pp. 312–321.
- 746 [26] M. J. MUCKLEY, B. RIEMENSCHNEIDER, A. RADMANESH, S. KIM, G. JEONG, J. KO, Y. JUN, H. SHIN,  
747 D. HWANG, M. MOSTAPHA, ET AL., *Results of the 2020 fastmri challenge for machine learning mr image*  
748 *reconstruction*, IEEE transactions on medical imaging, 40 (2021), pp. 2306–2317.
- 749 [27] M. MURPHY, M. ALLEY, J. DEMMEL, K. KEUTZER, S. VASANAWALA, AND M. LUSTIG, *Fast  $\ell_1$ -SPIRiT com-*  
750 *pressed sensing parallel imaging MRI: Scalable parallel implementation and clinically feasible runtime*, IEEE  
751 Transactions on Medical Imaging, 31 (2012), pp. 1250–1262.
- 752 [28] K. P. PRUESSMANN, M. WEIGER, M. B. SCHEIDEGGER, AND P. BOESIGER, *SENSE: sensitivity encoding for fast*  
753 *MRI*, Magnetic Resonance in Medicine, 42 (1999), pp. 952–962.
- 754 [29] G. K. RAFAEL REISENHOFER, SEBASTIAN BOSSE AND T. WIEGAND, *A haar wavelet-based perceptual similarity*  
755 *index for image quality assessment*, Signal Processing: Image Communication, 61 (2018), pp. 33–43.
- 756 [30] O. RONNEBERGER, P. FISCHER, AND T. BROX, *U-net: Convolutional networks for biomedical image segmentation*,  
757 in Medical Image Computing and Computer-Assisted Intervention–MICCAI 2015: 18th International Confer-  
758 ence, Munich, Germany, October 5–9, 2015, Proceedings, Part III 18, Springer, 2015, pp. 234–241.
- 759 [31] P. J. SHIN, P. E. Z. LARSON, M. A. OHLIGER, M. ELAD, J. M. PAULY, AND A. M. L. DANIEL B. VIGNERON,  
760 *Calibrationless parallel imaging reconstruction based on structured low-rank matrix completion*, Magnetic Reso-  
761 nance in Medicine, 725 (2014), pp. 959–970.
- 762 [32] A. SRIRAM, J. ZBONTAR, T. MURRELL, A. DEFAZIO, C. L. ZITNICK, N. YAKUBOVA, F. KNOLL, AND P. JOHN-  
763 SON, *End-to-end variational networks for accelerated mri reconstruction*, in Medical Image Computing and  
764 Computer Assisted Intervention–MICCAI 2020: 23rd International Conference, Lima, Peru, October 4–8, 2020,  
765 Proceedings, Part II 23, Springer, 2020, pp. 64–73.
- 766 [33] M. UECKER, P. LAI, M. J. MURPHY, P. VIRTUE, M. ELAD, J. M. PAULY, S. S. VASANAWALA, AND M. LUSTIG,  
767 *ESPIRiT-an eigenvalue approach to autocalibrating parallel MRI: where SENSE meets GRAPPA*, Magnetic Reso-  
768 nance in Medicine, 71 (2014), pp. 990–1001.
- 769 [34] M. UECKER AND M. LUSTIG, *Estimating absolute-phase maps using esprit and virtual conjugate coils*, Magnetic  
770 Resonance in Medicine, 77 (2017), pp. 1201–1207.
- 771 [35] C. P. B. A. V. ANTUN, F. RENNA AND A. C. HANSEN, *On instabilities of deep learning in image reconstruction*  
772 *and the potential costs of ai*, Proceedings of the National Academy of Sciences, 117 (2020), pp. 30088–30095.
- 773 [36] S. WANG, S. TAN, Y. GAO, Q. LIU, L. YING, T. XIAO, Y. LIU, X. LIU, H. ZHENG, AND D. LIANG, *Learning*  
774 *joint-sparse codes for calibration-free parallel MR imaging*, IEEE Transactions on Medical Imaging, 37 (2018),  
775 pp. 251–261.
- 776 [37] D. S. WELLER, J. R. POLIMENI, L. GRADY, L. L. WALD, E. ADALSTEINSSON, AND V. K. GOYAL, *Sparsity-*  
777 *promoting calibration for GRAPPA accelerated parallel MRI reconstruction*, IEEE Transactions on Medical  
778 Imaging, 32 (2013), pp. 1325–1335.
- 779 [38] Y. XIAO AND X. ZHUANG, *Adaptive directional haar tight framelets on bounded domains for digraph signal repre-*  
780 *sentations*, Journal of Fourier Analysis and Applications, 27 (2021), pp. 1–26.
- 781 [39] M. YAN, *A new primal-dual algorithm for minimizing the sum of three functions with a linear operator*, Journal of  
782 Scientific Computing, 76 (2018), pp. 1698–1717.
- 783 [40] G. YANG, S. YU, H. DONG, G. SLABAUGH, P. L. DRAGOTTI, X. YE, F. LIU, S. ARRIDGE, J. KEEGAN, Y. GUO,  
784 AND D. FIRMIN, *Dagan: Deep de-aliasing generative adversarial networks for fast compressed sensing MRI*  
785 *reconstruction*, IEEE Transactions on Medical Imaging, 37 (2017), pp. 1310–1321.
- 786 [41] Y. YANG, J. SUN, H. LI, AND Z. XU, *Deep ADMM-Net for compressive sensing MRI*, in Proceedings of the 30th  
787 International Conference on Neural Information Processing Systems, 2016, pp. 10–18.
- 788 [42] M. YASHTINI, *Euler’s elastica-based algorithm for parallel MRI reconstruction using SENSitivity encoding*, Opti-  
789 mization Letters, 14 (2020), pp. 1435–1458.
- 790 [43] X. YE, Y. CHEN, AND F. HUANG, *Computational acceleration for MR image reconstruction in partially parallel*  
791 *imaging*, IEEE Transactions on Medical Imaging, 30 (2011), pp. 1055–1063.
- 792 [44] L. YING AND J. SHENG, *Joint image reconstruction and sensitivity estimation in SENSE (JSENSE)*, Magnetic Reso-  
793 nance in Medicine, 57 (2007), pp. 1196–1202.
- 794 [45] J. ZBONTAR, F. KNOLL, A. SRIRAM, T. MURRELL, Z. HUANG, M. J. MUCKLEY, A. DEFAZIO, R. STERN,  
795 P. JOHNSON, M. BRUNO, ET AL., *fastMRI: An open dataset and benchmarks for accelerated MRI*, arXiv preprint  
796 arXiv:1811.08839, (2018).